

1 **Reconstruction of Climate-Driven Global Terrestrial Water Storage**
2 **Variations (2002–2021) Using a Four-Parameter Linear Recursive**
3 **Model**

4 **Pu Xie, Shuang Yi***

5 National Key Laboratory of Earth System Numerical Modeling and Application,
6 College of Earth and Planetary Sciences, University of Chinese Academy of
7 Sciences, Beijing, 101408, China

8 * Corresponding email: s.yi@ucas.ac.cn

9

10 Abstract

11 Terrestrial water storage anomalies (TWSA), jointly influenced by climatic variability and
12 human activities, ~~serve as a key indicator of global climate change.~~ TWSA exhibits pronounced
13 fluctuations across multiple temporal scales, ~~and~~ a substantial portion of ~~which the fluctuations can be~~
14 ~~be~~ attributed to climatic variability, ~~such as~~ like the El Niño–Southern Oscillation (ENSO). Empirical
15 reconstruction of climate-driven water storage based on relationships between GRACE satellite
16 gravity observations and meteorological forcing data has become a common approach; however,
17 existing models often neglect the regulating role of temperature in the transformation of
18 precipitation into water storage. In this study, we propose a linear, four-parameter coupled recursive
19 model that explicitly incorporates temperature effects on both the conversion and dissipation
20 efficiency of water storage. Using GRACE/GRACE-FO satellite observations and meteorological
21 forcing data, we reconstructed climate-driven TWSA over the global land grid (excluding Antarctica)
22 at a ~~daily~~ monthly temporal resolution and 0.5° spatial resolution for the period 2002 to 2021. For
23 116 major global river basins, we further derived basin-scale TWSA reconstructions and
24 quantitatively evaluated the fraction of precipitation converted into TWSA. ~~Finally, the~~
25 ~~reconstructed data were compared with existing reconstruction datasets.~~ Compared with existing
26 statistical reconstruction products, the results indicate that: (1) the proposed method achieves
27 substantially faster parameter convergence, improving computational efficiency by several tens of
28 times during the TWSA reconstruction process; (2) the proposed model demonstrates superior
29 performance in approximately 89% of river basins and 62% of global land grid cells. ~~Specifically,~~
30 ~~the Nash–Sutcliffe efficiency (NSE) exceeds 0.7 in 84 out of 116 basins, and 62% of global land~~
31 ~~grids exhibit NSE values greater than 0.~~ Additional comparisons with the physically based
32 Catchment Land Surface Model (CLSM) product from NASA’s Global Land Data Assimilation
33 System (GLDAS) show that the proposed method better captures the temporal variability of GRACE
34 TWSA in most basins. At the daily scale, the reconstructed TWSA agrees well overall with the
35 ITSG-Grace2018 daily solution and GLDAS-2.2. ~~In addition, our reconstruction demonstrates~~
36 ~~comparable performance during independent training and validation periods, indicating good~~
37 ~~robustness and limited overfitting.~~ This study enhances the understanding of the mechanisms
38 governing terrestrial water storage variations at both global and regional scales, provides a
39 quantitative assessment of climate-driven water storage changes, and offers a solid foundation for
40 disentangling the respective impacts of climatic variability and human activities on water resources.

41 **Keywords: GRACE, GRACE-FO, Reconstruction, TWSA, Climate variability**

43 **1 Introduction**

44 Terrestrial water storage (TWS) is the total amount of water stored in all components, including
45 surface water (e.g., lakes and reservoirs), groundwater, soil moisture, snow and ice, and vegetation
46 water, and it plays a vital role in the global hydrological cycle. Monitoring TWS is essential not only
47 for understanding the climate system and its variability (Tapley et al., 2019), but also for supporting
48 industrial development and ensuring global food security (Abbott et al., 2019; Rodell et al., 2009;
49 Rodell et al., 2018). Temperature and precipitation are the primary climatic drivers of TWS
50 variations. For instance, precipitation anomalies induced by ENSO are a dominant cause of
51 interannual TWS variability (Liu et al., 2020; Ni et al., 2018).

52 Traditionally, changes in TWS have been estimated using two main approaches. The first is the
53 water balance method, which requires precipitation, evapotranspiration, and runoff data.
54 Precipitation is typically measured by rain gauges, evapotranspiration is monitored using eddy
55 covariance systems (Baldocchi et al., 2001; Pastorello et al., 2020; Ma et al., 2024), and runoff is
56 estimated from discharge records at hydrological gauging stations (Duan et al., 2024). The rate of
57 TWS change ($dTWS/dt$) is then inferred from the water balance ~~Equation~~ Equation. However, because
58 ground-based observation stations are spatially discrete, this method can only provide localized,
59 point-scale information. In regions constrained by limited financial resources or political barriers to
60 data access, the sparse distribution of monitoring sites further hinders the establishment of
61 continuous spatial coverage (Crochemore et al., 2020; Fekete et al., 2012; Laudon et al., 2017). The
62 second is the model-based approach, in which land surface or hydrological models simulate
63 individual storage components such as soil moisture and groundwater, which are then aggregated to
64 estimate total TWS variations. However, both instrumental and measurement errors can propagate
65 through the modeling process, introducing substantial uncertainties into the final TWS estimates
66 (Long et al., 2015; Humphrey et al., 2023). Moreover, the uncertainty associated with hydrological
67 model outputs remains difficult to quantify (Zheng et al., 2023).

68 Since its launch in 2002, the Gravity Recovery and Climate Experiment (GRACE) mission has
69 provided precise measurements of temporal variations in Earth's gravity field and delivered monthly
70 gravity field solutions (Tapley et al., 2019; Chen et al., 2022; Humphrey et al., 2023). Compared
71 with traditional approaches that rely on sparse ground-based observations or hydrological models
72 with large uncertainties, GRACE data have substantially improved the spatial continuity and
73 observational reliability of Earth's gravity measurements, providing a crucial tool for monitoring
74 global water storage changes. A major contributor to temporal variations in the terrestrial gravity
75 field is the variations in TWS, which is jointly driven by natural climate variability, long-term

76 climate change, and human water use (Rodell et al., 2018; An et al., 2021). Distinguishing
77 anthropogenic signals from natural variability in GRACE-observed TWS has therefore become an
78 active research focus (An et al., 2021; Liu et al., 2021; Yi et al., 2016; Zhang et al., 2025).

79 Currently, reconstruction methods for climate-driven TWSA can be broadly classified into two
80 categories. The first category is data-driven approaches, which establish nonlinear mappings
81 between GRACE-based TWSA and climate–hydrological variables using machine learning or
82 neural network models (Fan et al., 2021; Palazzoli et al., 2025; Li et al., 2021; Sun et al., 2020;
83 Zhang et al., 2016; Long et al., 2014; Sun et al., 2021; Yin et al., 2023; Li et al., 2020). The advantage
84 of such approaches lies in their ability to capture complex patterns without requiring prior
85 assumptions about the underlying physical processes (Long et al., 2014) and without being
86 constrained by the spatial resolution of the input drivers. For instance, Zhang et al. (2016)
87 reconstructed TWSA in the Yangtze River Basin for the period from 1979 to 2012 using an artificial
88 neural network driven by precipitation and ERA-Interim soil moisture, and subsequently estimated
89 drought recovery times. Sun et al. (2021) introduced an automated machine learning framework for
90 GRACE-based TWSA reconstruction, integrating GLDAS model outputs together with
91 meteorological and climatic predictors to combine physical constraints with data-driven learning.
92 Palazzoli et al. (2025) developed unidirectional and bidirectional Long Short-Term Memory
93 networks to construct four climate-driven models, generating a continuous global TWSA record at
94 0.5° resolution for the period from 1984 to 2021. Li et al. (2021) combined statistical analysis, time
95 series decomposition, and machine learning techniques to reconstruct global (excluding Antarctica)
96 gridded TWSA for the period from 1979 to 2020 using multiple predictors, such as sea surface
97 temperature and climate indices. Yin et al. (2023) also adopted this approach and incorporated a
98 broader range of predictors in addition to conventional climatic variables, including land use data
99 and vegetation indices, to reconstruct a continuous global monthly TWSA dataset at 0.5° spatial
100 resolution for the period 1940 to 2022.

101 The second category of methods involves data-driven statistical models for reconstructing
102 TWSA (Zhong et al., 2019; Zhong et al., 2025; Humphrey and Gudmundsson, 2019; Xiao et al.,
103 2025). Humphrey and Gudmundsson (2019) proposed a statistical reconstruction approach that uses
104 only precipitation and temperature as predictors to estimate climate-driven TWS at both daily and
105 monthly time scales over the past century. Their method not only successfully filled the ~ 1 -year
106 observational gap between the GRACE and GRACE-FO missions but also demonstrated
107 performance comparable to or exceeding that of several global hydrological models. However, their
108 model incorporates a mathematical fitting procedure to align the reconstructed TWSA with GRACE

109 observations. This adjustment improves amplitude consistency but does not provide a clear physical
 110 interpretation. Building on this framework, Zhong et al. (2025) introduced a key modification by
 111 incorporating the concept of the “mean daily fraction of precipitation converted to TWS”, thereby
 112 adding a physically interpretable representation of the precipitation-to-storage transformation
 113 process. Based on this enhancement, they re-estimated that approximately 64% of terrestrial
 114 precipitation contributed to TWS across 121 global river basins during the period from 2002 to 2021,
 115 with substantial spatial variability linked to climatic and geographic conditions. The specific
 116 formulations and reconstruction workflows of both statistical models are detailed in Sections 3.1
 117 and 3.2 of this study.

118 Expanding upon the frameworks of Humphrey and Gudmundsson (2019) and Zhong et al.
 119 (2025), this study further advances parameter design. Whereas previous models relied on two
 120 empirical parameters in a residence-time formulation that is only indirectly linked to individual
 121 water-balance components without clear physical meaning, we propose a linear, four-parameter
 122 coupled recursive model at the daily time scale. This model explicitly incorporates temperature
 123 modulation of both the immediate infiltration-conversion efficiency of precipitation and, as well as
 124 the retention rate of water storage and its temperature sensitivity. The model includes four
 125 parameters, all of which have clear physical interpretation. The four model parameters are designed
 126 to be more closely tied to these hydrological processes. Detailed interpretations of the parameters
 127 are provided in Section 3.2.1. In addition, the approach has been optimized for computational
 128 efficiency and numerical stability. Using this method, we reconstructed a global (excluding
 129 Antarctica) gridded TWSA dataset at 0.5° spatial resolution and monthly time step for the period
 130 from 2002 to 2021 (the product name is provided in Section 4.1). The reconstructed TWSA closely
 131 matches GRACE observations and achieves accuracy levels comparable to or exceeding those of
 132 existing reconstruction products, as demonstrated in comprehensive benchmark evaluations.

133

134 **2 Data**

135 **Table 1 List of the data sets**

Dataset	Time	Spatial resolution	Temporal resolution
GSFC RL06v2.0 mascon solution	2002—2021	1°equal area (provided on 0.5°)	monthly

JPL CRI Filtered RL06.1v03 mascon solution	2002— 2021 2023	3.0°equal area (provided on 0.5°)	monthly
<u>CSR RL06v2.0 mascon solution</u>	<u>2002—2021</u>	<u>1°equal area (provided on 0.25°)</u>	<u>monthly</u>
Precipitation (ERA5-land)	2000— 2023 5	0.1°	hourly
Precipitation (MSWEP v2.8)	2000—2021	0.1°	daily
Temperature (ERA5-land)	2000— 2023 5	0.1°	hourly
Temperature (GLDAS-v-2.2)	2003—2021	0.25°	daily
Evapotranspiration (ERA5-land)	2000—2020	0.1°	hourly
<u>TWS (GLDAS CLSM)</u>	<u>2003—2021</u>	<u>1°</u>	<u>monthly</u>
<u>TWSA (GLDAS-2.2)</u>	<u>2003—2021</u>	<u>0.25°</u>	<u>daily</u>
GRACE-REC (Humphrey’s reconstruction)	2002—2019	0.5°	monthly

136

137 2.1 GRACE data

138 This study employs ~~two~~three GRACE/GRACE-FO mascon solutions (Table 1): the JPL RL06
139 v03 mascon product (JPLM) provided by the Jet Propulsion Laboratory (Wiese et al., 2019), the
140 CSR RL06 v2.0 mascon product (CSRM) provided by the Center for Space Research (Save et al.,
141 2016), —and the GSFC RL06v2.0 mascon product (GSFCM) provided by the NASA Goddard Space
142 Flight Center (Loomis et al., 2019). All datasets cover the period from 2002 to 2021. The native
143 resolution of JPLM is $3^\circ \times 3^\circ$ equal-area caps, and the data are distributed on a 0.5° latitude and
144 longitude grid. The GSFCM product has a native resolution of $1^\circ \times 1^\circ$ equal-area caps and is also
145 provided on a 0.5° grid. Both mascon products have been preprocessed with geocenter correction,

146 degree-2 replacement, and GIA correction, and thus require no further post-processing-(Zhang and
147 Sun, 2022).

148 **2.2 Precipitation and Temperature Data**

149 This study employs two precipitation products and two temperature products (Table 1). For
150 precipitation, the following datasets are used: (1) The ERA5-Land dataset, developed by the
151 European Centre for Medium-Range Weather Forecasts (ECMWF), is the land component of the
152 ERA5 reanalysis. It is driven by atmospheric forcing variables from ERA5 and provides hourly
153 precipitation data at a spatial resolution of $0.1^\circ \times 0.1^\circ$ (~9 km), covering the period from January
154 1950 to present (Muñoz-Sabater et al., 2021; Muñoz-Sabater, 2019); (2) The Multi-Source
155 Weighted-Ensemble Precipitation (MSWEP) version 2.8 dataset (Beck et al., 2017; Beck et al., 2019)
156 spans from 1979 to present and offers precipitation estimates at $0.1^\circ \times 0.1^\circ$ spatial resolution and
157 multiple temporal resolutions (3-hourly, daily, and monthly). In this study, the daily product is used.
158 MSWEP combines gauge observations, satellite retrievals, and reanalysis data using a weighted
159 ensemble approach to provide high-accuracy global precipitation estimates (Beck et al., 2017).

160 For temperature, the following datasets are used: (1) The ERA5-Land reanalysis dataset
161 produced by ECMWF (Muñoz-Sabater, 2019); (2) the GLDAS-2.2 daily CLSM product NASA's
162 Global Land Data Assimilation System (GLDAS) developed the GLDAS v2.2 Catchment Land
163 Surface Model (CLSM) product (Li et al., 2019). This model offers a physically based framework
164 suitable for assimilating GRACE-derived TWS observations. The GLDAS-v-2.2 dataset-daily
165 product includes both a main version and an early product. This study uses the main version, which
166 spans from February 2003 to July-December 2025-2021 (as of manuscript preparation), with a spatial
167 resolution of $0.25^\circ \times 0.25^\circ$ and a daily temporal resolution. It should be noted that, due to the data
168 usage agreement with the ECMWF, which prohibits redistribution of products from the Integrated
169 Forecasting System (IFS), the GLDAS-2.2 daily product does not include the meteorological forcing
170 fields. Instead, GLDAS-2.2 provides land surface variables simulated by the Catchment land surface
171 model, which is forced by meteorological analysis fields from the operational ECMWF IFS.

172 Although both ERA5-Land and GLDAS-2.2 are ultimately based on meteorological
173 information produced within the ECMWF framework, their temperature datasets exhibit a
174 discrepancy of approximately 1–2 °C (Fig. S1) due to different data assimilating methods and
175 models.

176 ERA5-Land precipitation and temperature are used as the primary meteorological inputs in this
177 study. The MSWEP precipitation and GLDAS-2.2 temperature datasets are additionally used to

178 compare standard deviations with ERA5-Land, in order to assess the uncertainty of ERA5-Land
179 forcing data and support the subsequent parameter uncertainty analysis.

180 **2.3 Ancillary Data**

181 This study employs basin boundaries from the publicly available dataset “Major River Basins
182 of the World” provided by the Global Runoff Data Centre (GRDC). This dataset has been widely
183 used in large-scale hydrological studies (e.g., Burek and Smilovic (2023); Zhong et al. (2025); Gao
184 et al. (2026)). We followed the strategy of Zhong et al. (2025) and ranked all basins according to
185 drainage area to ensure spatial representativeness and avoid subjective selection. The 116 largest
186 basins with drainage areas exceeding 10^5 km^2 were selected for analysis. This study selected 116
187 river basins, with basin boundaries obtained from the Global Runoff Data Centre (GRDC).

188 The classification of basin climate types was based on the mean annual aridity index, derived
189 from the Global Aridity Index and Potential Evapotranspiration Climate Database (Zomer et al.,
190 2022; Trabucco and Zomer, 2019), which is available in GeoTIFF format. The aridity index is
191 defined as the ratio of annual precipitation to mean annual potential evapotranspiration, where
192 higher values indicate more humid conditions. Climate types were categorized according to the
193 aridity index as follows: arid (aridity index < 0.2), semi-arid ($0.2 \leq$ aridity index < 0.5), semi-
194 humid ($0.5 \leq$ aridity index < 0.65), and humid (aridity index ≥ 0.65).

195

196 **3 Methods**

197 **3.1 Previous Statistical Models for TWSA Reconstruction**

198 **3.1.1 Humphrey’s Reconstruction Model**

199 Precipitation is the primary input to terrestrial water storage. Statistical models that reconstruct
200 TWSA from daily precipitation and temperature can be used to quantify the influence of climatic
201 variability on terrestrial water storage (Humphrey and Gudmundsson, 2019). For comparison
202 purposes, we first revisit the statistical reconstruction model proposed by Humphrey and
203 Gudmundsson (2019) :

$$204 \quad TWS(t) = TWS(t-1) \cdot e^{-\frac{1}{\tau(t)}} + P(t). \quad (1)$$

205 Here ~~where~~ t is the daily time index, $TWS(t)$ is the water storage on day t , $P(t)$ is the
206 precipitation input on day t , and $\tau(t)$ is the water residence time. A larger τ implies slower losses

207 through evapotranspiration or runoff, while a smaller τ indicates faster depletion.

208 $\tau(t)$ is defined as a function of temperature to represent the seasonal variations in water
209 residence time.

$$210 \quad \tau(t) = a + b \cdot T_z(t), \quad (2)$$

211 ~~where with~~ a and b are model parameters to be calibrated.

212 To reduce the influence of extreme temperatures on model stability, the original temperature
213 $T(t)$ is first detrended and standardized, then transformed using a sigmoid function:

$$214 \quad T_z = 1 - \tanh\left(\frac{T_0 - \text{mean}(T_0)}{\text{SD}(T_0)}\right). \quad (3)$$

215 Since subzero temperatures have negligible effects on residence time (as temperature changes
216 exert little influence on storage losses such as evapotranspiration and runoff under freezing or
217 insufficient thawing conditions), the original temperature series $T(t)$ was preprocessed as follows:

$$218 \quad T_0 = \begin{cases} 0, & T < 0 \\ T, & T \geq 0 \end{cases}. \quad (4)$$

219 The initial water storage $TWS(0)$ is computed as the ratio of long-term mean precipitation to
220 mean water loss rate:

$$221 \quad TWS(0) = \frac{\text{mean}(P)}{1 - \text{mean}\left(e^{-\frac{1}{\tau(t)}}\right)}. \quad (5)$$

222 The daily TWS series is aggregated to monthly means $TWS(t_m)$ and calibrated against
223 deseasonalized and detrended GRACE TWSA at the monthly scale. The model parameters
224 a, b and β are calibrated using a Markov Chain Monte Carlo (MCMC) approach, with the objective
225 of minimizing the sum of squared residuals between the simulated and GRACE-derived TWSA:

$$226 \quad \text{anom}(GRACE(t_m)) = \beta \cdot \text{anom}(TWS(t_m)) + \epsilon. \quad (6)$$

227 The coefficient β serves as a scaling factor obtained from MCMC calibration, ϵ denotes the
228 residual term, and $\text{anom}(\cdot)$ represents the anomaly series after removal of the seasonal cycle and
229 linear trend.

230 **3.1.2 Zhong's Reconstruction Model**

231 The scaling factor β in Eq. (6) lacks clear physical meaning and serves merely as a calibration
232 parameter, resulting in a strong dependence of the reconstruction on GRACE observations. Building
233 on this framework, Zhong et al. (2025) proposed an improved formulation for reconstructing
234 terrestrial water storage :

$$235 \quad TWS(t) = TWS(t-1) \cdot e^{-\frac{1}{\tau(t)}} + \beta \cdot P(t). \quad (7)$$

236 In this formulation, the parameter β has a clear physical interpretation, representing the mean
 237 fraction of daily precipitation that contributes to water storage. The residence time $\tau(t)$ is defined
 238 as in Eq. (2). It is important to note that this β is fundamentally different from the scale factor used
 239 in Eq. (6).

240 The daily TWS series is aggregated to monthly means $TWS(t_m)$ and calibrated against
 241 deseasonalized and detrended GRACE TWSA at the monthly scale. The model parameters
 242 a, b and β are also calibrated using the MCMC approach:

$$243 \quad \text{anom}(GRACE(t_m)) = \text{anom}(TWS(t_m)) + \epsilon. \quad (8)$$

244 Owing to the high nonlinearity of the estimation model, parameter optimization is prone to
 245 being trapped in local optima. To reduce the bias caused by incomplete chain convergence, the
 246 MCMC calibration was repeated 50 times for each basin. All parameter sets falling within the $\pm 1 \cdot$
 247 σ range were retained, and their averages were taken as the final estimates of parameters a, b and β .
 248 The standard deviation of these filtered parameters was then calculated to represent the inter-basin
 249 uncertainty of β .

250 **3.2 Proposed Reconstruction Method**

251 **3.2.1 Model formulation**

252 The two preceding approaches describe the residence time (Eq. 2) as a temperature-dependent
 253 function. However, the parameters a and b in Eq. (1) and (7) ~~its definition~~ are obtained by
 254 calibration, and they are less directly linked to specific water-balance components. ~~are merely~~
 255 ~~calibration coefficients without explicit physical meaning when substituted into the exponential~~
 256 ~~decay function (Eq. 1 and 7).~~ In this study, our model is derived directly from the basin-scale water
 257 balance equation and provided a systematic clarification of both the derivation and the physical
 258 interpretation of the parameters. ~~we propose a linearized modification of the water storage~~
 259 ~~reconstruction formula, which simultaneously accounts for the temperature-regulated memory term~~
 260 ~~$TWS(t - 1)$,~~ and the temperature-dependent precipitation conversion rate, as follows:

261 We start from the water balance equation:

$$262 \quad TWS(t) - TWS(t - 1) = P(t) - ET(t) - R(t) = P(t) - ETR(t), \quad (9)$$

263 where $P(t)$, $ET(t)$, and $R(t)$ denote precipitation, evapotranspiration, and runoff at time
 264 step t , respectively, and $ETR(t) = ET(t) + R(t)$ represents the total loss term. We assume that
 265 ETR consists of two components: (1) the contemporaneous precipitation loss ETR_1 , i.e., the direct
 266 loss occurring as precipitation is converted into water storage; and (2) the storage-release loss ETR_2 ,
 267 i.e., the loss arising from the depletion of antecedent water storage $TWS(t - 1)$ in subsequent

268 periods, which can be expressed as

$$269 \quad ETR_1(t) = x \cdot P(t), \quad (10)$$

$$270 \quad ETR_2(t) = y \cdot TWS(t - 1), \quad (11)$$

$$271 \quad ETR(t) = ETR_1(t) + ETR_2(t) = x \cdot P(t) + y \cdot TWS(t - 1). \quad (12)$$

272 The assumption is validated in Fig. S2, where the ETR is plotted against precipitation and
273 TWS respectively. Both plots show significant correlations, with ETR apparently exhibiting a
274 stronger correlation with the current precipitation than the antecedent TWS .

275 We then performed a multiple linear regression analysis to further test this assumption. In this
276 step, temperature modulation was temporarily ignored and the coefficients x and y were treated
277 as constants. The results show that all basins pass the F-test at the significance level of $p < 0.01$.
278 Moreover, 74 basins (approximately 64% of all basins) exhibit determination coefficients $R^2 > 0.6$
279 (Fig. S3(a)), indicating that the total loss term ETR can be statistically explained by the linear
280 combination of precipitation $P(t)$ and antecedent storage $TWS(t - 1)$.

281 We compared the full multiple regression model with a reduced model that includes only
282 precipitation $P(t)$ as the predictor to further examine whether antecedent storage $TWS(t - 1)$
283 provides additional explanatory power beyond precipitation alone. Figure S3(b) presents the spatial
284 distribution of the R^2 obtained from the precipitation-only regression, while Fig. S3(c) shows the
285 spatial difference in R^2 between the full model and the reduced model. Although precipitation alone
286 explains a substantial portion of the variability in basin-scale losses, the inclusion of antecedent
287 storage $TWS(t - 1)$ improves model performance. Across all basins, the incorporation of
288 $TWS(t - 1)$ increases R^2 by approximately 0.1. Therefore, although ETR is strongly correlated
289 with $P(t)$, the results demonstrate that accounting for $TWS(t - 1)$ is both statistically meaningful
290 and physically necessary.

291 On this basis, we consider the modulation effect of temperature on the hydrological cycle by
292 assuming that the proportional coefficients x and y vary with temperature and apply a Taylor
293 expansion, which yields

$$294 \quad x = \epsilon \cdot f(T_z) = \epsilon \cdot (1 + \alpha T_z + o(T_z^2)). \quad (13)$$

295 Retaining only the first-order approximation gives

$$296 \quad x = a' \cdot T_z + b', \quad (14)$$

297 where T_z denotes standardized temperature.

298 Similarly, we obtain

$$299 \quad y = c' \cdot T_z + d'. \quad (15)$$

300 Substituting Eqs. (12), (14), and (15) into the water balance equation (Eq. 9) leads to

$$TWS(t) = (1 - a' \cdot T_z - b') \cdot P(t) + (1 - c' \cdot T_z - d') \cdot TWS(t - 1). \quad (16)$$

After merging constant terms simplifying the signs, the recursive formulation adopted in this study is obtained as

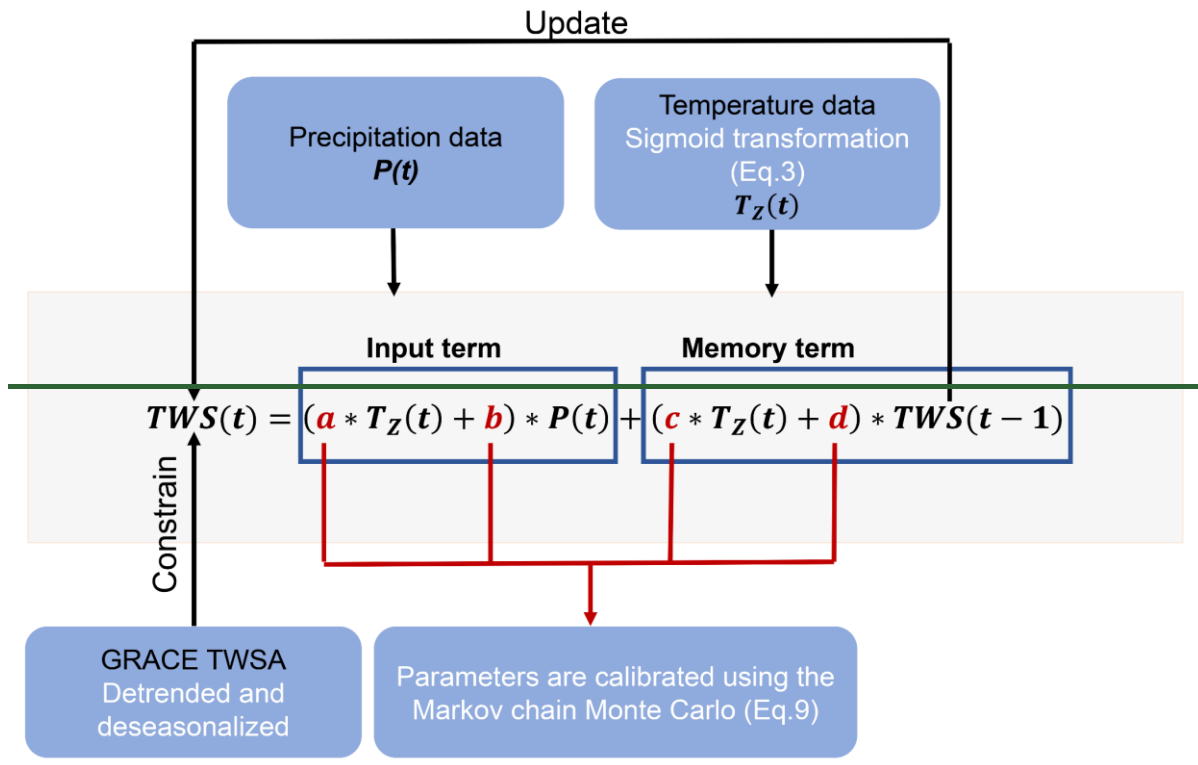
$$TWS(t) = (a \cdot T_z + b) \cdot P(t) + (c \cdot T_z + d) \cdot TWS(t - 1), \quad (17)$$

which is the reconstruction model adopted in this study. In this form, parameters a and c represent temperature modulation effects. The term $1 - b$ can be interpreted as the fraction of precipitation that directly contributes to the loss component $ETR_1(t)$; therefore, parameter b represents the effective proportion of precipitation that contributes to TWS after basin losses. Similarly, $1 - d$ represents the fraction of antecedent storage contributing to the loss term $ETR_2(t)$, and thus parameter d represents the fraction of previous storage retained in the current storage state. We will continue to discuss these parameters in subsequent sections.

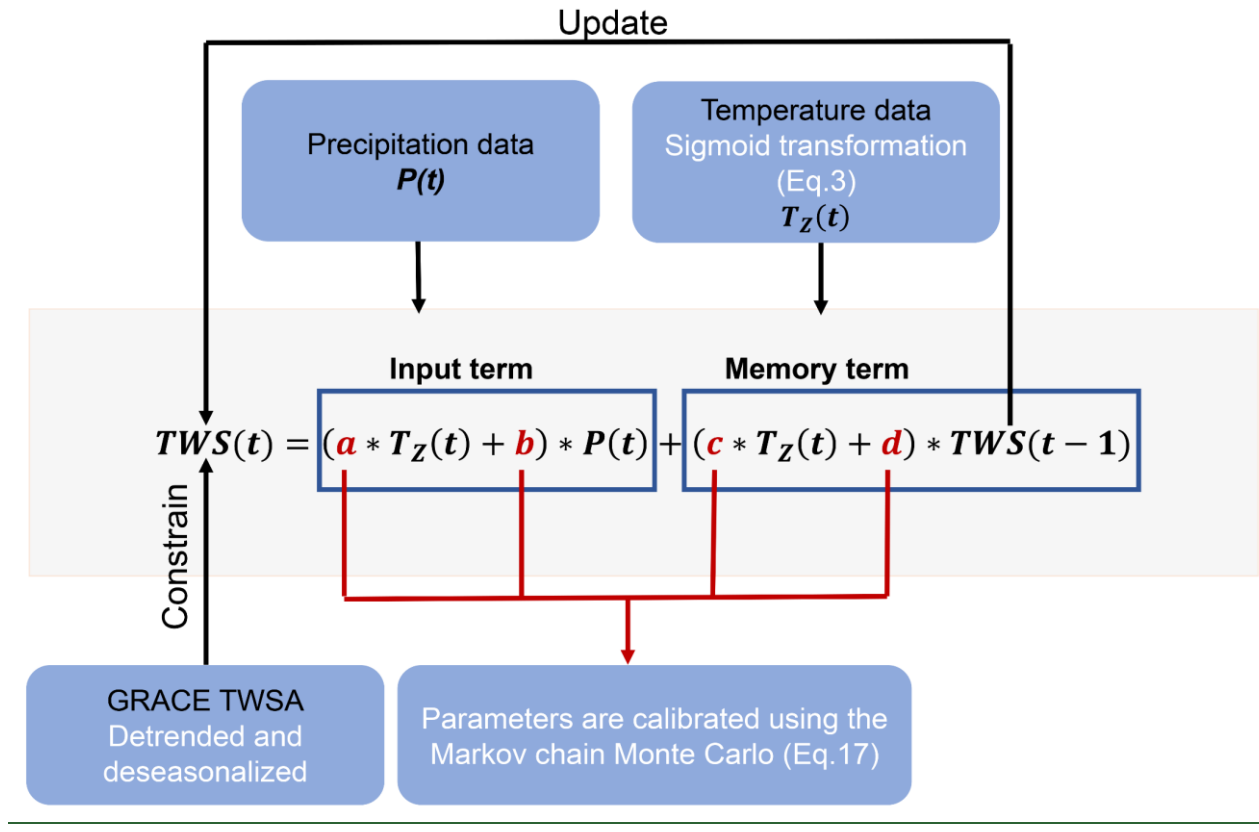
All four parameters in the Eq. are endowed with clear physical interpretations. Specifically, parameter a reflects the regulating effect of temperature on the conversion of precipitation into water storage. Parameter b represents the proportion of precipitation that directly contributes to TWS when $T_z = 0$. Parameter c quantifies the temperature-mediated influence of antecedent water storage $TWS(t - 1)$ on current storage $TWS(t)$. Parameter d represents the proportion of storage retained from the previous time step that is independent of temperature variations.

When solving Eq. (1), (7), and (9), it is necessary to specify the initial water storage value, $TWS(0)$. Humphrey and Gudmundsson (2019) and Zhong et al. (2025) assumed that the initial water storage corresponds to an equilibrium state, as defined in Eq. (5). Although using Eq. (5) provides a unique and reproducible starting condition, it inherently assumes that water storage is close to equilibrium at the beginning of the reconstruction period. However, if a basin experiences an extreme hydroclimatic condition at the initial time step, adopting Eq. (5) may introduce systematic biases and consequently affect the MCMC calibration of other parameters. In this study, $TWS(0)$ is also treated as a variable and is simultaneously estimated together with other model parameters through a joint least-squares and MCMC optimization. This approach eliminates the need to assume equilibrium conditions at the start of the reconstruction period and is therefore more suitable for basins under nonequilibrium states, such as those influenced by prolonged droughts or intensive groundwater extraction (see Section 5.1.2 for details).

The calibration procedure in this section follows exactly the same steps as described in Section 3.1.2, with Eq. (8) retained throughout the process. The reconstruction logic of TWSA is illustrated in Fig. 1.



333



334

335 Figure 1: Illustration of the physical meaning of parameters.

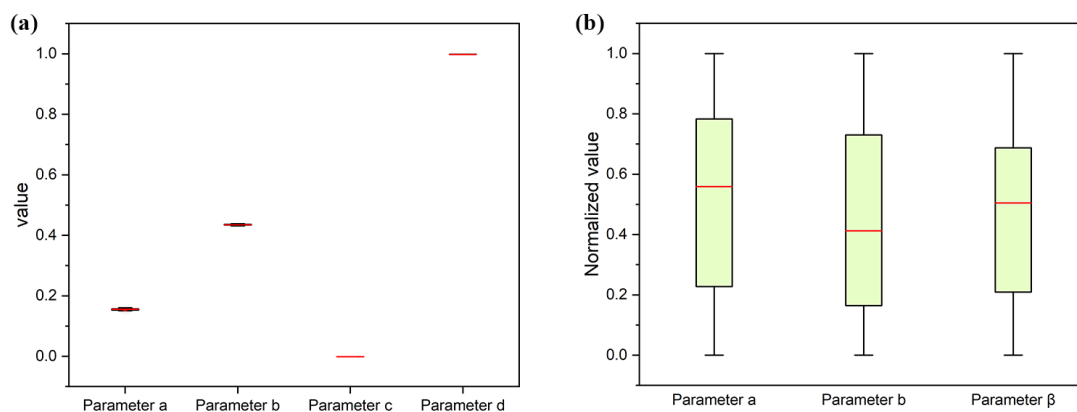
336 Compared with the methods of Humphrey and Gudmundsson (2019) and Zhong et al. (2025),
 337 this study linearizes the memory term $TWS(t - 1) \cdot e^{-\frac{1}{\tau(t)}}$ as $(c \cdot T_z + d) \cdot TWS(t - 1)$. A key

338 advantage of this linearization is its computational stability and rapid convergence, which
 339 substantially improves inversion efficiency. Under the same parameter calibration framework as
 340 Zhong et al. (2025), both our model and the Zhong’s model were run with 50 independent MCMC
 341 chains for the Yellow River to derive the posterior parameter distributions. The parameter dispersion
 342 (indicated by the box height) in our model (Fig. 2a) is considerably narrower than that in Zhong’s
 343 model (Fig. 2b), indicating that our model exhibits smaller parameter uncertainties and faster chain
 344 convergence. Consequently, a single MCMC calibration is sufficient for each basin in our method,
 345 greatly reducing computation time without a noticeable loss of fitting accuracy. Specifically, on our
 346 computing platform (Intel 13th Gen Core i9-13900H processor, 14 cores, base frequency 2.60 GHz,
 347 turbo frequency up to ~ 5.4 GHz, and 16 GB RAM), the Zhong’s model required 50 parameter
 348 calibrations, taking a total of 353.8 s for a single basin, whereas our method required only one
 349 calibration, completing the computation in 6.8 s.

350 In summary, this study improves upon previous models in three aspects:

- 351 (1) Linearization of the memory term. The linearization not only accelerates computational
 352 performance but also enhances the physical interpretability of parameters.
- 353 (2) Incorporation of the coupling between temperature and precipitation. This mechanism
 354 adjusts the fraction of precipitation converted into water storage, leading to a slight
 355 improvement in NSE across most basins and substantial enhancement in several cases (see
 356 Section 5.2.2).
- 357 (3) Consideration of the impact of different initial values on model fitting results (see Section
 358 5.1.2).

359



360 Figure 2: Comparison of parameter stability in the Yellow River Basin between (a) our reconstruction model and
 361 (b) the model of Zhong et al. (2025), based on 50 independent calibrations using the MCMC approach. Parameter
 362 medians (red lines) are highlighted.

363 3.2.2 Further interpretation of Our Equations

364 To demonstrate the compatibility of the proposed model with existing approaches, we consider
 365 two extreme cases:

366 (1) In the model of Zhong et al. (2025), the memory factor is expressed as $e^{-\frac{1}{\tau(t)}}$. When
 367 applying a first-order Taylor expansion to the exponential term in Eq. (7), it can be approximated
 368 as:

$$369 \quad TWS(t) = \beta \cdot P(t) + \left(1 - \frac{1}{\tau(t)}\right) \cdot TWS(t-1). \quad (180)$$

370 Our model (Eq. 917) becomes mathematically similar to Eq. (180) when the temperature and
 371 precipitation modulation is neglected (i.e., $a = 0$). This indicates that our model degenerates to the
 372 first-order linear form of the Zhong model when temperature effects are not considered.

373 (2) Assuming that the memory term is unaffected by temperature ($c = 0$) and exhibits perfect
 374 conversion efficiency ($d = 1$), Eq. (917) simplifies to:

$$375 \quad TWSC(t) = TWS(t) - TWS(t-1) = (a \cdot T_z + b) \cdot P(t). \quad (191)$$

376 The water balance Eq. is given as:

$$377 \quad TWSC(t) = P(t) - ET(t) - R(t). \quad (2012)$$

378 This implicitly assumes a proportional linear relationship between the loss terms, $ET(t) +$
 379 $R(t)$, and the precipitation input $P(t)$: $R(t) + ET(t) = (1 - a \cdot T_z - b) \cdot P(t)$. In other words,
 380 the total output is controlled by the input, so even without explicitly representing the loss terms, the
 381 Eq. is still able to account for their integrated contribution.

382 3.2.3 Uncertainty Estimation

383 To quantify the uncertainty associated with meteorological forcing data, this study estimates
 384 observational errors based on the differences between multiple data sources. Specifically, the
 385 standard deviation of daily precipitation differences between ERA5-Land and MSWEP is used as
 386 the uncertainty estimate for ERA5-Land precipitation, while the standard deviation of daily
 387 temperature differences between ERA5-Land and GLDAS-GLSM is used to estimate the
 388 uncertainty in ERA5-Land temperature.

389 Temperature uncertainty:

$$390 \quad \sigma_T = std(T_{ERA5-Land} - T_{GLDAS-GLSM}). \quad (2113)$$

391 Precipitation uncertainty:

392
$$\sigma_P = std(P_{\text{ERA5-Land}} - P_{\text{MSWEP}}). \quad (2314)$$

393 Building on this, we adopt a Monte Carlo simulation framework in which Gaussian noise with
394 zero mean and standard deviations of σ_T and σ_P is added to the temperature and precipitation
395 inputs, respectively. For each perturbed dataset, the model is recalibrated to obtain an optimal set of
396 parameters under the given realization. After completing 1,000 simulations, all sets of estimated
397 parameters are collected to derive the uncertainty distributions of both the model parameters and the
398 reconstructed TWS.

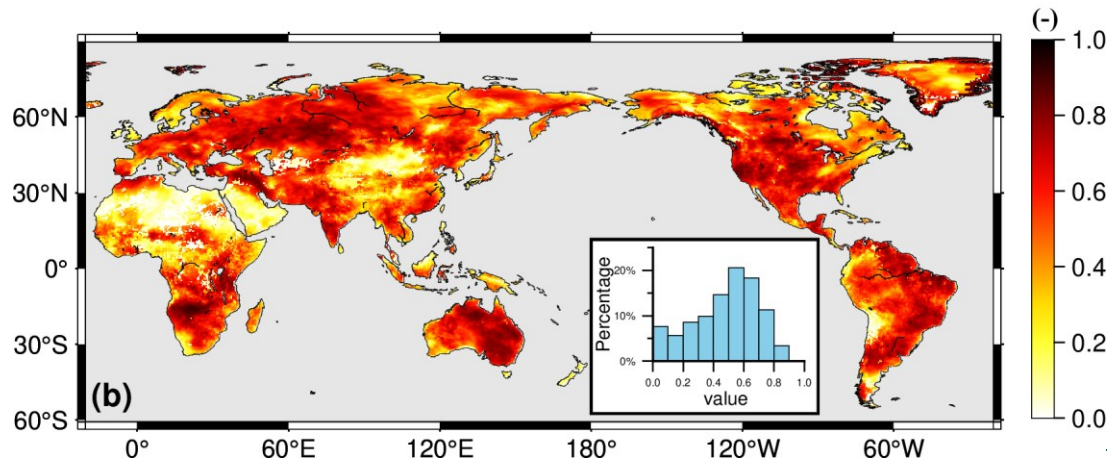
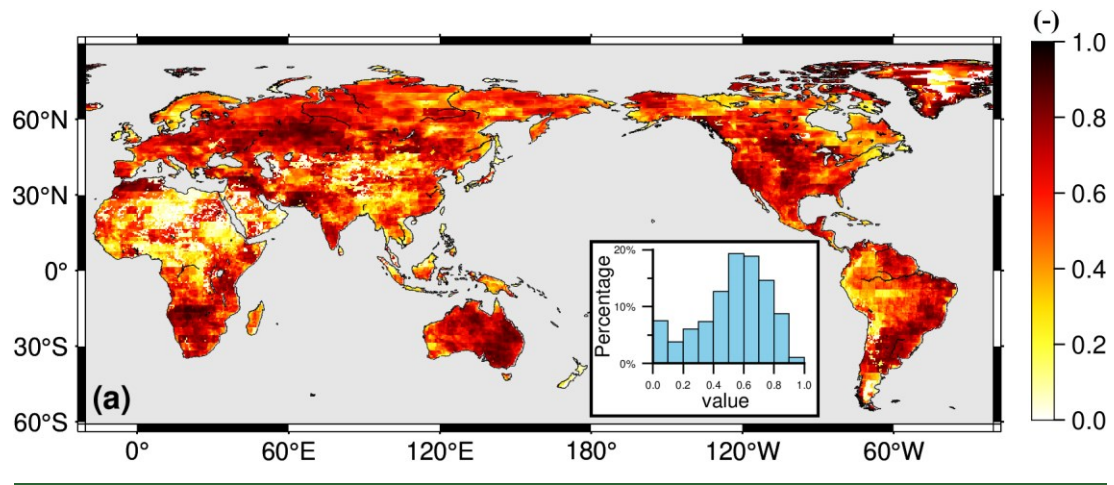
399

400 4 Results

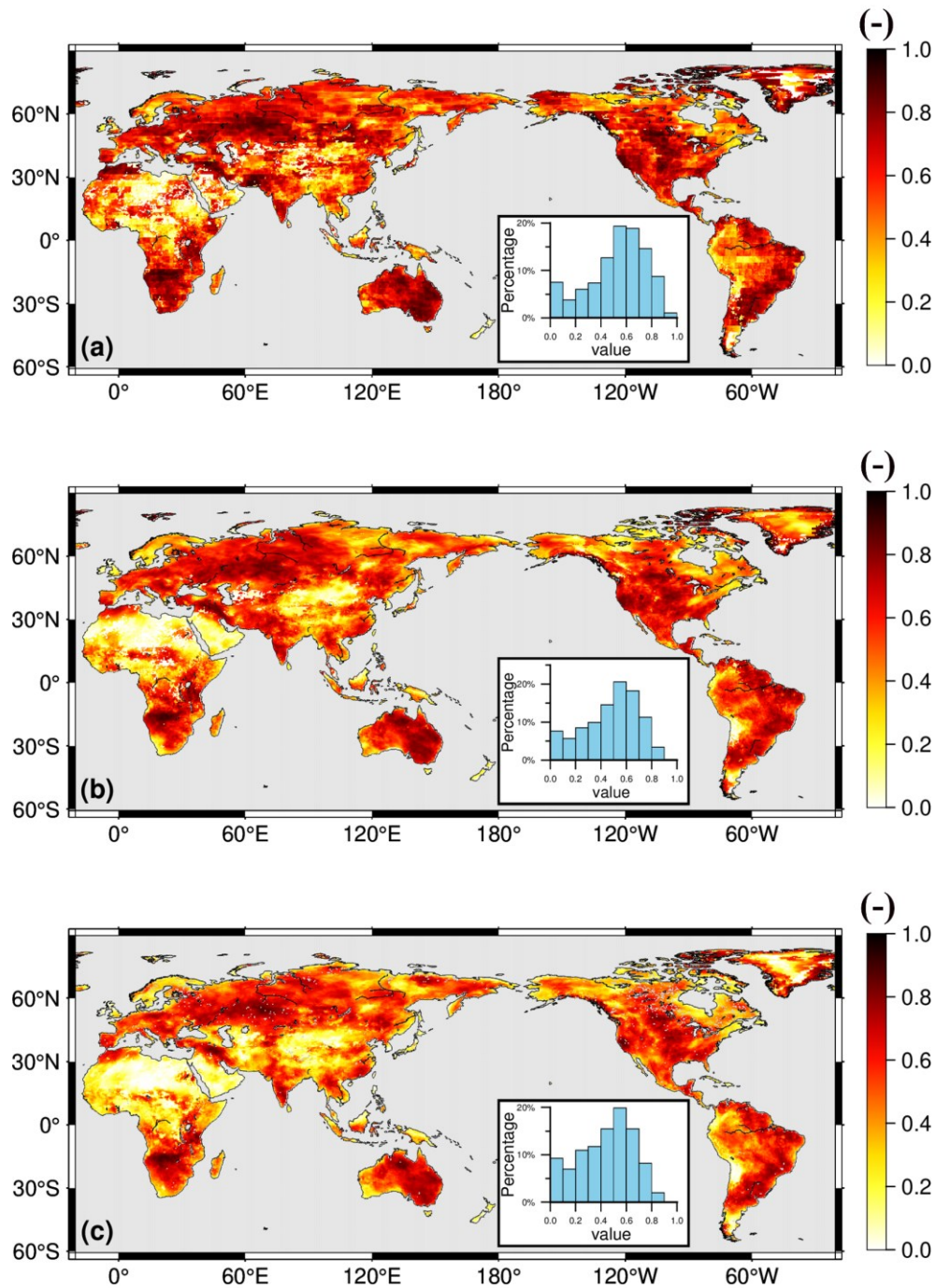
401 4.1 Performance summary

402 The performance of the GRACE reconstruction model was evaluated using the *NSE*. Figure 3
403 presents the spatial distribution of *NSE* values for 116 major river basins worldwide, and the
404 corresponding numerical results are provided in Table S1. For the reconstruction calibrated against
405 the JPLM product (hereafter referred to as JPL-REC), 53.3% of the 0.5° grid cells exhibited
406 *NSE* values in the range of 0.5 to 0.8, while 8.6% showed *NSE* > 0.8. High *NSE* values were
407 primarily concentrated in mid- to high-latitude regions such as North America, Europe, and
408 Australia, where in situ meteorological observations are relatively dense (Fig. 3a). In contrast,
409 regions such as most of Africa and the arid plateau zones of Central Asia showed relatively low
410 *NSE* values, likely due to the scarcity of precipitation and temperature observations (Xu et al., 2020;
411 Chen et al., 2008). The reconstruction calibrated against the GSFC mascon product (hereafter
412 GSFC-REC) displayed a spatial pattern broadly similar to that of JPL-REC, with 50.2% of grid cells
413 falling within the range from 0.5 to 0.8 and ~~2.8~~2.79% exceeding *NSE* > 0.8. We also compared
414 the reconstruction calibrated against the CSR product (hereafter referred to as CSR-REC) with
415 the CSR product to further evaluate robustness of the reconstruction method. The spatial
416 distribution of *NSE* (Fig. 3c) is broadly consistent with those obtained for JPL-REC and GSFC-
417 REC. The *NSE* distributions derived from the three mascon-based calibrations are largely
418 consistent, indicating that the reconstruction approach exhibits limited sensitivity to the source of
419 the mascon products, which is consistent with findings reported in previous studies~~The high spatial~~
420 ~~concordance of *NSE* between JPL-REC and GSFC-REC indicates that the reconstruction method is~~
421 ~~largely insensitive to the source of the mascon product, consistent with previous findings~~

422 (Humphrey and Gudmundsson, 2019).



423



424

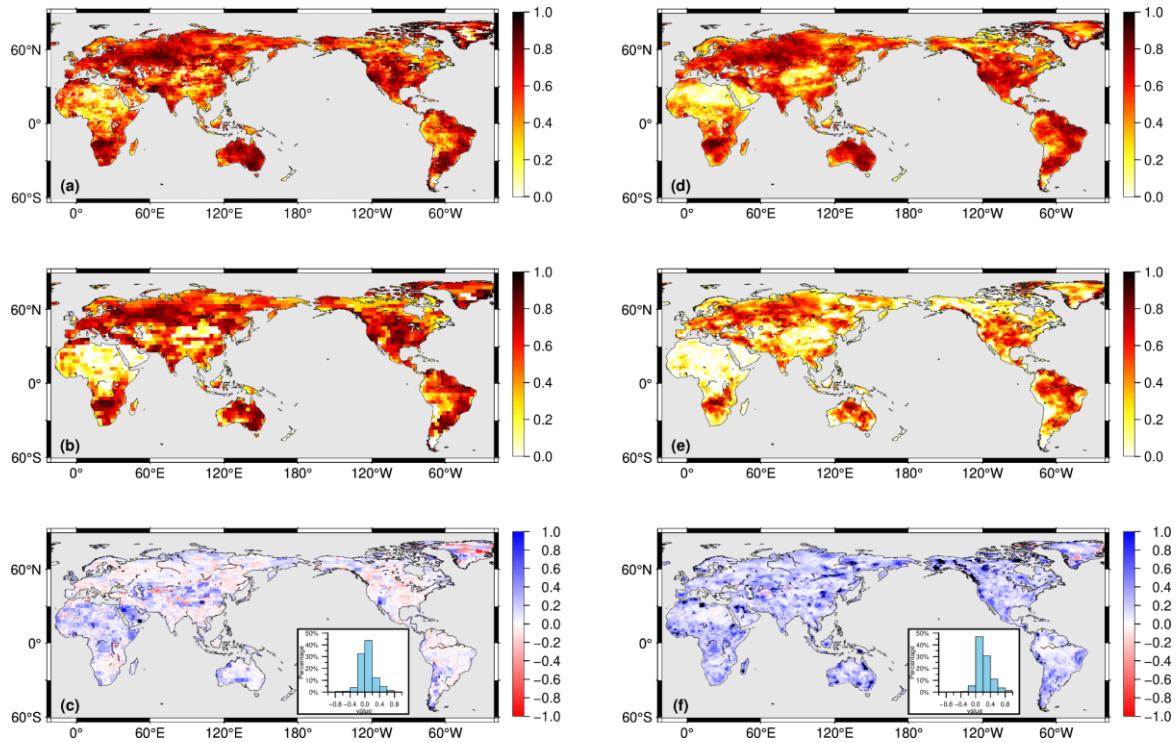
425 Figure 3: Spatial distribution of *NSE* (of de-seasonalized, de-trended anomalies) between our reconstruction and
 426 (a) *JPLM₂*, (b) *GSFCM₂*, and (c) *CSR_M* for the period from 2002 to 2021. Histograms show the distribution of
 427 *NSE* values across all global grid points.

428 4.2 Comparisons

429 4.2.1 Comparison with the Humphrey's Model

430 At the grid scale, we first compared the reconstruction results from this study (*JPL-REC* and

431 GSFC-REC) with those of Humphrey and Gudmundsson (2019), which were trained using the
432 JPLM and GSFCM products, respectively (hereafter referred to as Humphrey-JPL-REC and
433 Humphrey-GSFC-REC). Figure 4 presents the spatial distribution of NSE values between the
434 reconstructed and GRACE-derived TWSA after deseasonalization and detrending over the period
435 from 2002 to 2019. Figure 4a and 4d show the NSE performance of JPL-REC and GSFC-REC
436 relative to their corresponding mascon products (JPLM and GSFCM), respectively. Both panels
437 indicate high model performance ($NSE > 0.7$) across large parts of North America, Europe,
438 Australia, and southern Africa, whereas low NSE values ($NSE < 0.4$) are evident in parts of North
439 Africa, Central Asia, and the Arabian Peninsula. Figure 4b and 4e show the NSE performance of
440 Humphrey-JPL-REC and Humphrey-GSFC-REC relative to their corresponding mascon products
441 (JPLM and GSFCM), respectively. While the overall spatial patterns are broadly similar to those in
442 Fig. 4a and 4d, the extent of low-performance areas in Africa and Central Asia is noticeably larger
443 in the Humphrey reconstructions. Figure 4c and 4f present the differences in NSE (ΔNSE),
444 calculated as Fig. 4a minus Fig. 4b and Fig. 4d minus Fig. 4e, respectively. Blue shading ($\Delta NSE >$
445 0) indicates regions where the present method outperforms the approach by Humphrey and
446 Gudmundsson (2019). Notably, in Fig. 4c, approximately 63% of the grid cells show $\Delta NSE > 0$,
447 with substantial improvements in regions such as the Arabian Peninsula and sub-Saharan Africa,
448 along with scattered enhancements across other continents. Figure 4f demonstrates that under
449 GSFCM constraints, the present method substantially outperforms that of Humphrey and
450 Gudmundsson (2019). One potential explanation lies in the difference in training datasets: while
451 (Humphrey and Gudmundsson, 2019) utilized the GSFC mascon v2.4 (an older version that is no
452 longer publicly available), the present study employs the updated GSFC mascon RL06v2.0. This
453 difference may account for the discrepancies between our results in Fig. 4e and those reported in the
454 original publication by Humphrey and Gudmundsson (2019).



455

456 Figure 4: Spatial distribution of NSE (of de-seasonalized, de-trended anomalies) for the period from 2002 to
 457 2019. (a) and (d): NSE of JPL-REC and GSFC-REC against their respective GRACE mascon solutions. (b) and
 458 (e): NSE of Humphrey-JPL-REC and Humphrey-GSFC-REC against the corresponding GRACE mascon
 459 solutions. (c) and (f): Spatial differences in NSE between our reconstruction and that of Humphrey and
 460 Gudmundsson (2019), both relative to the same GRACE mascon solution. Values larger than 0 indicate better
 461 performance of our method.

462

4.2.2 Basin-scale comparison ~~Comparison with the Zhong Model~~

463

We compare our reconstruction (JPL-REC) with two representative types of products to systematically evaluate model performance at the basin scale: (1) a previous GRACE-based reconstruction product (Zhong-REC from (Zhong et al., 2025)), and (2) physically based land surface model simulations forced by meteorological data (GLDAS CLSM).

467

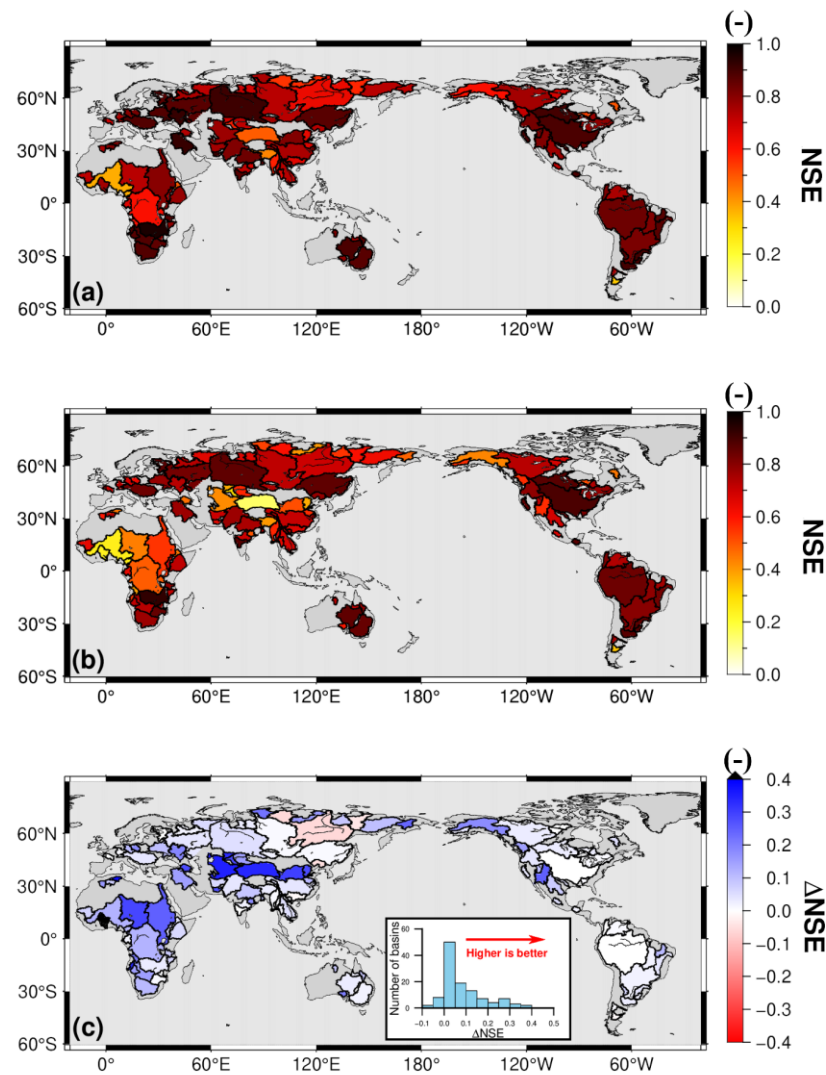
First, we adopted the JPLM as a common reference to evaluate the relative performance of different statistical reconstruction methods. We compared basin-averaged monthly TWSA from our JPL-REC and Zhong-REC against the JPLM and computed the NSE for each (Fig. 5). By comparing the NSE values for the two approaches, we assessed their relative reconstruction accuracy. We further compared the reconstruction results at the basin scale with those from Zhong et al. (2025). In the comparison across 116 major global river basins, ~~the our~~ proposed model achieved a median NSE of 0.76, outperforming ~~Zhong-REC the reconstruction by Zhong et al. (2025) (hereafter referred to as Zhong REC)~~, which had a median NSE of 0.70. Among these basins, 84 (73%)

474

475 achieved $NSE > 0.7$, compared to only 59 (51%) for Zhong-REC. Model performance was closely
476 linked to the quality of the forcing data and the dominant hydrological processes (Yi et al., 2023).
477 Poor performance ($NSE < 0.5$) was observed in basins such as the Congo, Niger, and Sanaga in
478 Africa, and the Tarim River in Central Asia, where sparse ground-based meteorological observations
479 result in large uncertainties in climate forcing data (Xu et al., 2020; Chen et al., 2008). Cold-region
480 basins such as the Yukon, Brahmaputra, Lena, Indigirka, Kolyma, Olenek, Yana, and Khatanga are
481 strongly influenced by glacial and permafrost-driven seasonal accumulation and ablation processes
482 (Riegger and Tourian, 2014; Yi et al., 2023). The linear reservoir assumption fails to adequately
483 capture the mass variations in these basins (Liu et al., 2022), resulting in NSE values ranging from
484 0.45 to 0.70. In contrast, river basins where hydrological signals are dominant, such as the Amazon,
485 Mississippi, Nelson, and Amur, showed good reconstruction performance with NSE values greater
486 than 0.80. The histogram of ΔNSE (this model minus Zhong-REC) shown in Fig. 5c reveals a
487 positively skewed distribution, indicating performance improvements in the majority of basins.
488 Specifically, 37 basins (approximately one-quarter of the sample) exhibited $\Delta NSE > 0.1$. The most
489 pronounced improvements were found in arid and semi-arid regions (Fig. S2S4), including the
490 Tarim River, Lake Chad, and Yellow River basins. The spatial distribution of regions with the most
491 notable improvements in Fig. 5c closely aligns with the ΔNSE pattern between the proposed model
492 and Humphrey-JPL-REC (Fig. S1S5), further supporting the role of the coupling between
493 temperature and precipitation and the joint inversion of initial conditions in enhancing
494 reconstruction accuracy in areas with low NSE .

495 Second, we compared basin-averaged monthly TWSA from JPL-REC and GLDAS CLSM to
496 highlight the improvement of our reconstruction method relative to the land surface model (Fig. S6).
497 Across 116 major river basins worldwide, NSE values for both products are computed against the
498 JPLM, and the spatial distribution of the resulting ΔNSE is presented (Fig. S6(c)). The results show
499 that NSE values from our reconstruction are higher in most basins, with ΔNSE predominantly
500 positive, indicating that the proposed method more effectively captures temporal TWSA variations
501 at the basin scale.

502 It should be noted that TWSA estimates from GLDAS CLSM are derived from explicit
503 simulations of individual storage components and are therefore influenced by the completeness and
504 accuracy of the represented physical processes. In contrast, our approach statistically characterizes
505 climate-driven storage responses under direct constraints from GRACE observations, implicitly
506 integrating multiple storage processes. This leads to improved representation of total water storage
507 variations and better agreement across many river basins.



509

510 Figure 5: Spatial distribution of *NSE* (de-seasonalized, de-trended anomalies) between JPL mascon and two
 511 reconstruction models across 116 global river basins for the period 2002 to 2021. The *NSE* between JPLM and
 512 JPL-REC (a); the *NSE* between JPLM and the reconstruction by Zhong et al. (2025) (b); and their difference
 513 ($\Delta NSE = JPL-REC - Zhong-REC$) (c). The inset histogram in (c) illustrates the distribution of ΔNSE across all
 514 basins, where positive values indicate better agreement with GRACE observations by our reconstruction model.

515 4.23.3 Comparison of Monthly Time Series

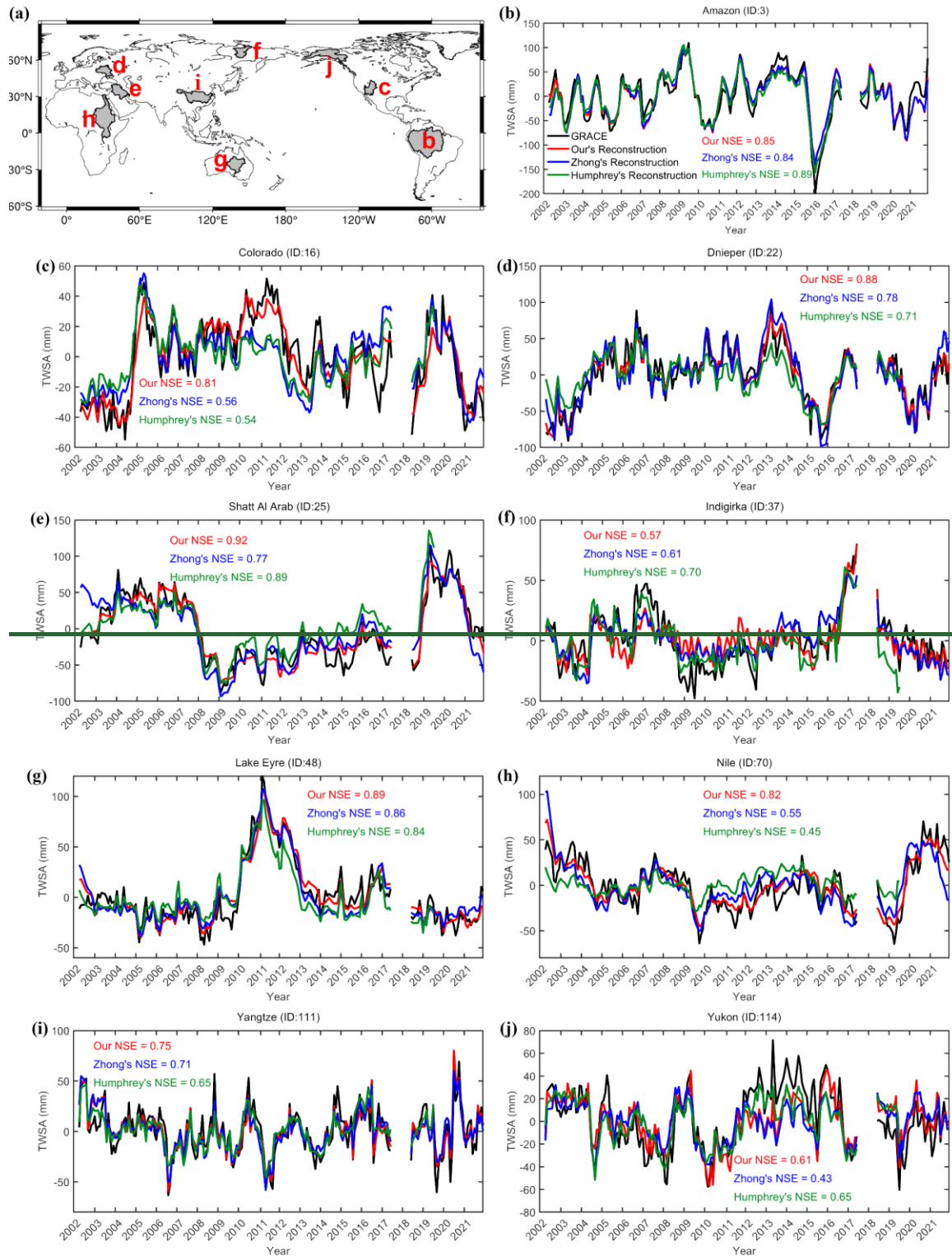
516 This section presents a comparison of deseasonalized and detrended monthly TWSA time
 517 series across ~~nine~~eight representative river basins. Figure 6 illustrates the differences among
 518 GRACE/GRACE-FO observations (black line), the present reconstruction (JPL-REC, red line),
 519 Zhong-REC (blue line), and Humphrey-JPL-REC (green line) in terms of basin-averaged TWSA
 520 time series.

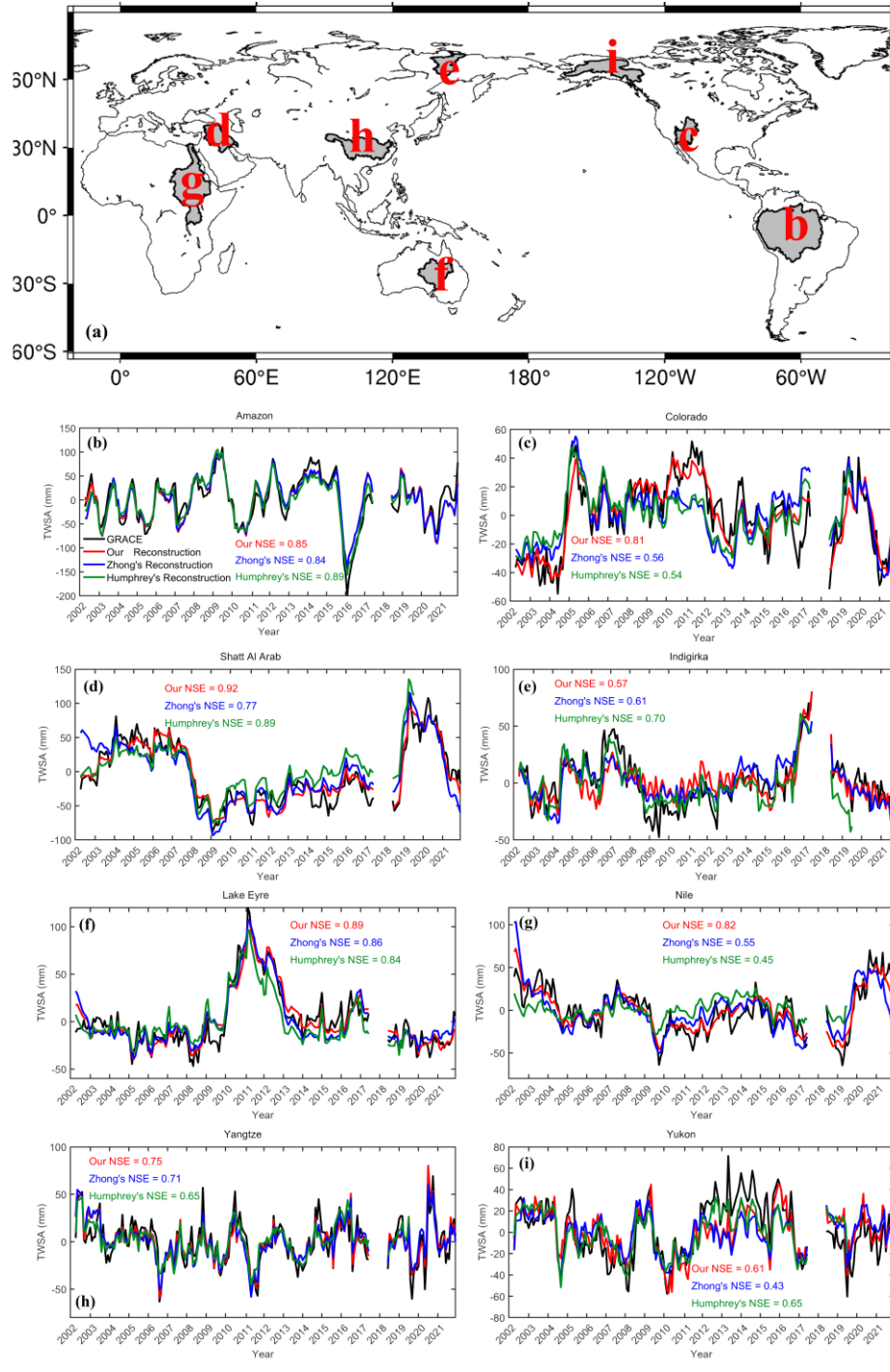
521 Interannual variations in terrestrial water storage are primarily driven by atmospheric

522 circulation anomalies induced by ENSO events, which often trigger hydrological extremes such as
523 floods and droughts, thereby significantly altering regional water balance (Chen et al., 2022). In the
524 Amazon Basin, the La Niña event of 2009 markedly increased regional precipitation (Chen et al.,
525 2010), while the strong El Niño of 2015–2016 led to severe drought conditions (Tian et al., 2021).
526 The proposed reconstruction model successfully captured both the water storage peak in 2009 and
527 the pronounced depletion in 2016. In the Yangtze River Basin, the early 2010 La Niña event was
528 one of the primary drivers of drought, as it weakened the East Asian summer monsoon and caused
529 an eastward retreat of the western Pacific subtropical high, thereby reducing moisture transport and
530 triggering drought in the middle and lower reaches (Li et al., 2023; Zhang et al., 2015). The sharp
531 decline in TWSA observed by GRACE during this period was accurately reproduced by the present
532 model. In the Nile Basin, due to the slower response of TWS compared to precipitation, the
533 reduction in net precipitation caused by the 2008 La Niña event did not immediately lead to a decline
534 in TWSA. Instead, TWSA exhibited a gradual downward trend from 2008 to 2010 (Forootan et al.,
535 2019), and this phase lag was also captured by the model. During the strong La Niña of the period
536 from 2010 to 2011, northern and inland Australia experienced abnormally wet conditions. In the
537 Lake Eyre Basin, intense rainfall and widespread flooding caused a significant rise in TWSA (Chen
538 et al., 2022). The reconstructed TWSA time series in this basin is highly consistent with GRACE
539 observations.

540 In contrast to the basins discussed above, interannual anomalies in river basins such as the
541 Colorado and Shatt al-Arab are closely coupled with human water extraction. In the Colorado Basin,
542 groundwater levels experienced a brief recovery from 2009 to 2010 due to increased precipitation.
543 However, an anomalous drought event in 2012, combined with record-low snowfall in the Rocky
544 Mountains, led to a rapid decline in water storage (Castle et al., 2014). Similarly, since the onset of
545 drought in 2007, the Shatt al-Arab Basin has experienced a sharp decline in precipitation,
546 compounded by a rapid drop in upstream reservoir levels along the Euphrates River. As surface
547 water supplies became insufficient to meet demand, groundwater abstraction surged and became the
548 primary source for agricultural and domestic use, leading to a rapid depletion of groundwater storage
549 (Voss et al., 2013). In the high-latitude Indigirka Basin, winter precipitation is primarily stored in
550 solid form, with snow water equivalent (SWE) gradually accumulating throughout the frozen season
551 and then melting intensively in the following summer. GRACE effectively captured this “snow
552 accumulation–melt” process, showing a spring peak of approximately 50 mm from 2006 to 2007.
553 By contrast, the four-parameter recursive model developed in this study treats all precipitation $P(t)$
554 as an immediate input flux, which is attenuated through a memory term $(c \cdot T_z + d) \cdot TWS(t - 1)$.

555 This assumption leads to premature dissipation of the snow accumulation signal during winter,
556 resulting in significant underestimation of the seasonal peak. Meanwhile, the relatively large
557 constant memory coefficient d caused part of the residual water to be released with a delay,
558 resulting in overall higher reconstructed TWSA compared to GRACE observations from 2008 to
559 2010. Among all basins examined, this basin exhibited the poorest performance of our method
560 relative to previous models.





562

563

Figure 6: Time series of GRACE/GRACE-FO TWSA and reconstructed TWSA, both de-seasonalized and de-

564

trended, for the nine-eight selected river basins (b-j) from 2002 to 2021. The global distribution of the nine-eight

565

selected river basins (a).

566

4.2.4 Comparison of Daily Time Series

567

Although our model is primarily constrained by monthly GRACE observations, the method

568

can also reconstruct daily characteristics in TWS changes based on the daily climate drivers. Here,

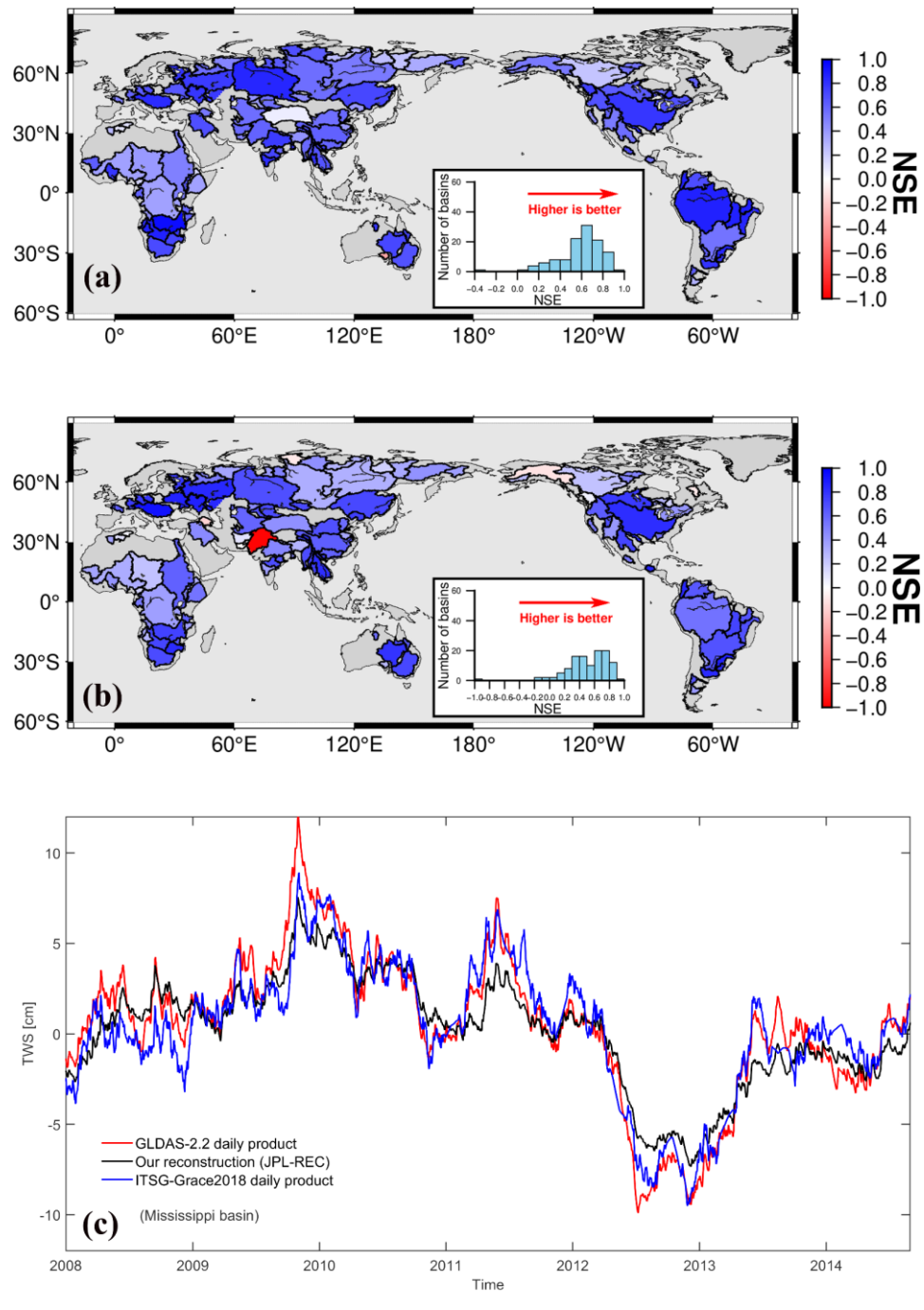
569

we evaluated our reconstructed daily TWSA by comparing it with two different reference datasets,

570 namely the daily ITSG-Grace2018 solution derived using a Kalman smoothing approach and the
571 GLDAS-2.2 Daily product. The comparison with ITSG-Grace2018 evaluates whether the daily
572 reconstruction is consistent with GRACE-based sub-monthly variability, whereas the comparison
573 with GLDAS-2.2 assesses whether the daily reconstruction is consistent with physically based land-
574 surface simulations.

575 We first assessed reconstruction performance at the basin scale by computing basin-averaged
576 daily TWSA over major river basins worldwide. The difference in the time series was quantified
577 using *NSE* (Fig. 7a&b). The *NSE* values are positive across most basins, with over half
578 exceeding 0.5, indicating that our reconstruction results align well with the previous models.
579 Although the reconstruction performs well overall relative to both reference datasets, its agreement
580 with ITSG-Grace2018 is stronger in many basins. Specifically, 63 basins show *NSE* values greater
581 than 0.6 in comparison with ITSG-Grace2018, whereas the count slightly reduces to 51 when
582 compared with GLDAS-2.2. This is likely because our reconstruction is calibrated under constraints
583 from GRACE/GRACE-FO TWSA, while ITSG-Grace2018 is also a daily product derived from
584 GRACE observations.

585 To better illustrate sub-monthly variability, we showed daily TWSA time series in the
586 Mississippi River basin in Fig. 7c. The results show similar sub-monthly variabilities among the
587 reconstructed GRACE-REC, ITSG-Grace2018, and GLDAS-2.2 time series. One exception is found
588 in the Indus basin between our GRACE-REC and GLDAS-2.2. The main reason is that GLDAS-2.2
589 fails to capture a three-year drought spanning from 2016 and 2018 (see Fig. S7 for details). The
590 reconstructed daily TWSA is consistent with the corresponding reduction in the 6-month moving
591 average of precipitation. By contrast, the GLDAS-2.2 daily TWSA remains comparatively flat
592 during this period, suggesting that it may underestimate the sensitivity of basin-scale storage to
593 interannual hydroclimatic forcing in this basin. Figure S7(b) further shows that our monthly
594 reconstruction remains close to the GRACE/GRACE-FO observations, particularly around the
595 resumption of GRACE-FO observations in June 2018, whereas GLDAS-2.2 tends to overestimate
596 TWSA at that time. This discrepancy highlights the indispensable role of observation-based
597 reconstruction approaches.



598

599 Figure 7: Spatial distribution of NSE (of de-seasonalized and de-trended TWSA) between our daily
 600 reconstruction and (a) ITSG-Grace2018 for the period from January 2003 to August 2016 and (b) the GLDAS-2.2
 601 daily product for the period from January 2003 to December 2021 across 116 major river basins worldwide. (c)
 602 Time-series comparison of the three daily datasets for the Mississippi River basin, focusing on the period 2008–
 603 2014 to improve the readability of high-frequency fluctuations.

604 **4.2.5 Independent validation of reconstruction performance**

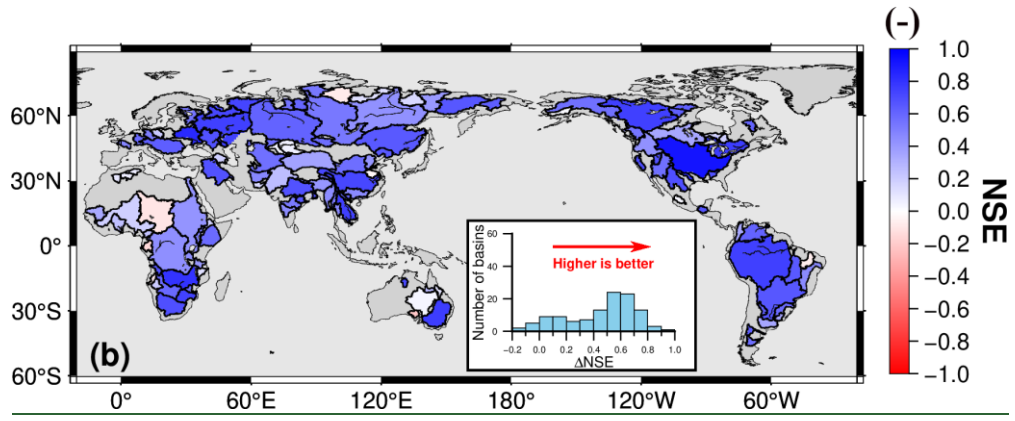
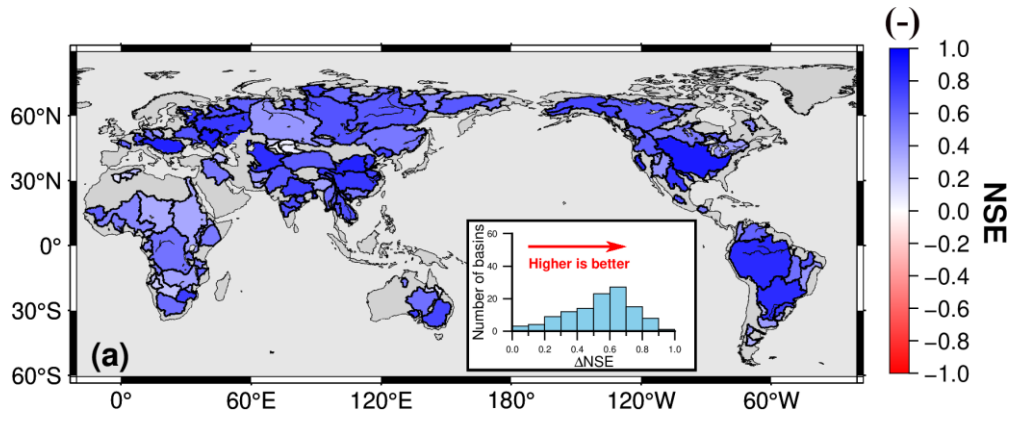
605 We conducted a self-validation experiment to further evaluate the robustness of the proposed
 606 method by dividing the JPLM product into separate training and validation periods. Specifically, the

607 period from April 2002 to December 2012 was designated as the training period and the model
608 parameters were estimated, while the period from January 2013 to December 2023 was treated as
609 an independent validation period.

610 We evaluated the model performance using the *NSE* by comparing JPL-REC with the JPLM
611 in both the training and validation periods (Fig. 8). During the training period (Fig. 8a), most basins
612 exhibit high reconstruction skill, with *NSE* values exceeding 0.6 over large parts of North and
613 South America as well as Eurasia. A very similar spatial pattern is obtained for the validation period
614 (Fig. 8b), with only a modest reduction in overall skill. Approximately 60 % of the basins retain
615 *NSE* values above 0.5 in the validation period. This indicates that the model retains stable predictive
616 capability beyond the calibration window and does not exhibit significant overfitting behavior.

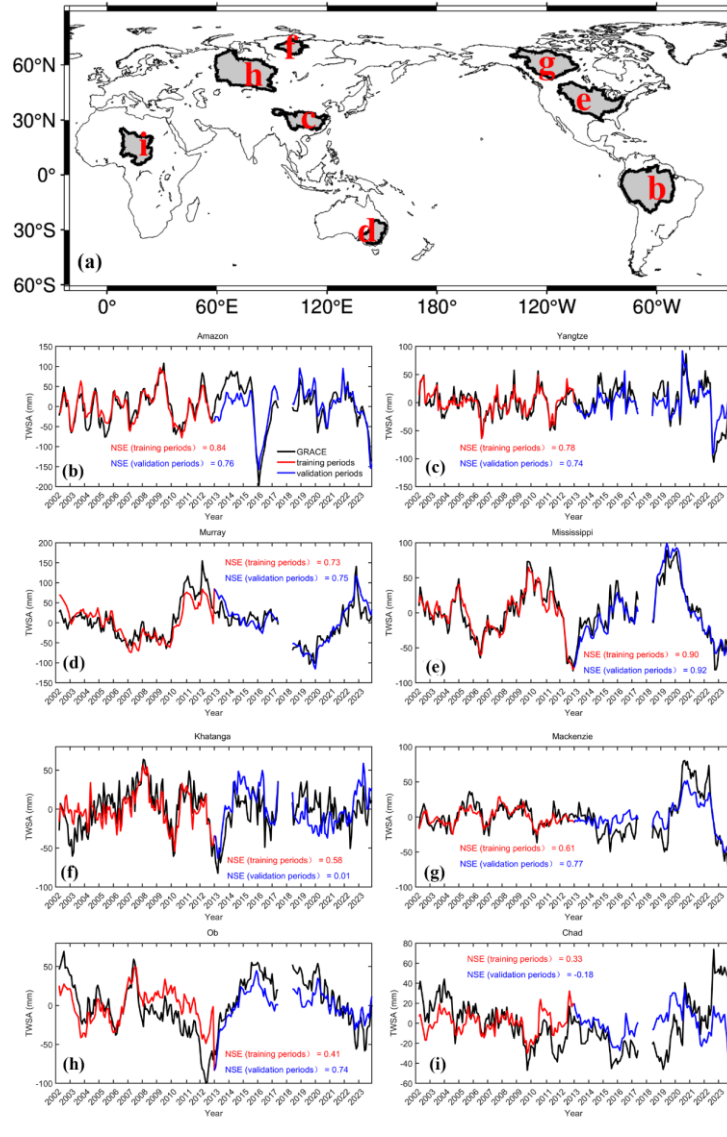
617 The spatial pattern of the results during validation period reveals distinct regional
618 characteristics. High *NSE* values are mainly found in large, humid basins with relatively dense
619 observations, such as the Amazon, Mississippi, Yangtze River basins. In these regions, variability
620 in TWS is strongly controlled by climate forcing. Consequently, our model can reliably reproduce
621 the TWSA signals observed by GRACE/GRACE-FO.

622 We further selected eight representative basins spanning high-latitude cold regions, tropical
623 humid regions and typical monsoon-affected areas (Fig. 9). For each basin, the validation period
624 TWSA (blue line) was compared with the reconstructed values during the training period (red line)
625 and GRACE observations (black line). The results show that in certain basins, such as the Amazon,
626 Yangtze, Mississippi and Murray, model performance during the extrapolation period remained
627 comparable to or even exceeded that during the training period. This indicates that under these
628 hydroclimatic conditions, the fixed-parameter model can reliably capture interannual TWSA
629 variability driven by precipitation and temperature. In contrast, basins such as Chad and Khatanga
630 show lower *NSE* during the validation period and larger discrepancies in certain years. This
631 decline may be attributed to the limitations imposed by parameter nonstationarity and errors in the
632 forcing data. These results suggest that when only precipitation and temperature forecasts are
633 available, the proposed recursive model can be directly applied for estimating TWS changes during
634 missing periods or into the future. Nevertheless, its applicability varies with hydroclimatic
635 conditions, and for regions requiring high prediction accuracy, periodic parameter updates or the
636 inclusion of additional forcing information may still be necessary.



637

638 Figure 8: Comparison of reconstruction performance against JPLM data during the training and validation periods.
 639 (a) Spatial distribution of the NSE between JPL-REC and JPLM data during the training period (April 2002–
 640 December 2012); (b) Spatial distribution of NSE during the validation period (January 2013–December 2023)



641
 642 Figure 9: Time series comparison of JPL-REC and JPLM, both de-seasonalized and de-trended, for the eight
 643 selected river basins (b-i) during training and validation periods. Black lines represent GRACE TWSA, red lines
 644 indicate model reconstructions during the training period, and blue lines during the validation period. The global
 645 distribution of the eight selected river basins (a).

646

647 5 Discussions

648 5.1 Sensitivity Analysis of the Model

649 5.1.1 Sensitivity to Temporal Resolution

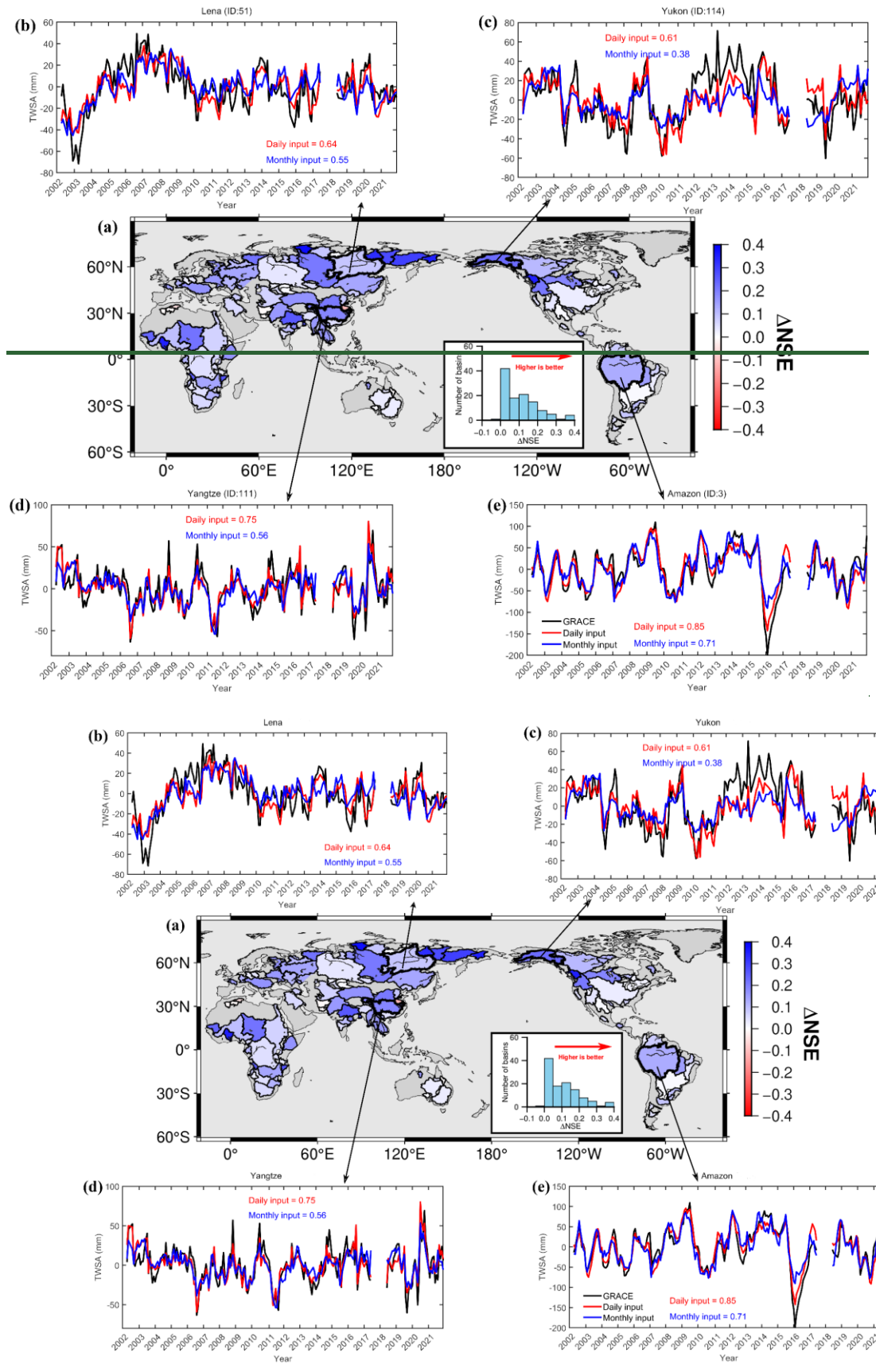
650 We first evaluated the impact of the temporal resolution of meteorological forcing data on
651 reconstruction performance, specifically whether daily forcing provides additional benefit compared
652 to monthly forcing. To this end, all 116 basins were recalibrated using both daily and monthly ERA5-
653 Land precipitation and temperature. The monthly forcing datasets were aggregated from daily values:
654 precipitation was summed to monthly totals, and temperature was averaged over each month. The
655 deseasonalized and detrended TWSA reconstructions were then compared on a monthly basis, and
656 NSE was computed for each case. The difference between the two forcing schemes was quantified
657 as $\Delta NSE = NSE_{Daily} - NSE_{Monthly}$, with its spatial distribution shown in Fig. 7a8a. Positive
658 values indicate better performance under daily forcing.

659 The results show that 108 out of 116 basins (approximately 95%) exhibit positive ΔNSE
660 values, suggesting that daily forcing generally outperforms monthly forcing. The most significant
661 improvements were observed in high-latitude permafrost–glacier transition zones such as Siberia
662 and Alaska. In contrast, tropical humid basins (e.g., the Paraná Basin) exhibited minimal differences
663 ($\Delta NSE \leq \pm 0.05$). Only seven basins (approximately 5%), such as the Huai River Basin, showed
664 slightly negative differences ($-0.1 < \Delta NSE < 0$), mostly located in regions with strong human
665 regulation or sparse observational data.

666 From a time series perspective, the reconstructed TWSA driven by monthly climate forcing
667 exhibits significantly lower amplitude compared to that driven by daily forcing. This is mainly due
668 to two factors: daily forcing preserves extreme precipitation events and high-frequency temperature
669 fluctuations on a day-to-day basis, allowing short-term water flux pulses to enter the recursive
670 system as sharp peaks. In contrast, monthly forcing involves pre-integrating or averaging over 30-
671 day precipitation and temperature records before inputting them into the model, which smooths out
672 extreme events and leads to underestimated amplitude in the simulations (Humphrey et al., 2016).
673 In addition, the memory coefficient calibrated at the daily time step typically ranges from $d_{day} \approx$
674 0.97 to 0.995, indicating very limited attenuation on a daily basis. When directly scaled to a
675 monthly time step, this corresponds to $d_{day}^{30} \approx 0.74$; alternatively, recalibration at the monthly scale
676 yields an equivalent memory coefficient of approximately $d_{day}^{30} \approx 0.7$ to 0.8. Both cases imply a
677 stronger low-pass filtering effect, which further dampens peak values and elevates troughs.

678
679

Therefore, we argue that daily forcing is essential for improving model fidelity across nearly all basins and should be considered necessary for accurate reconstruction.



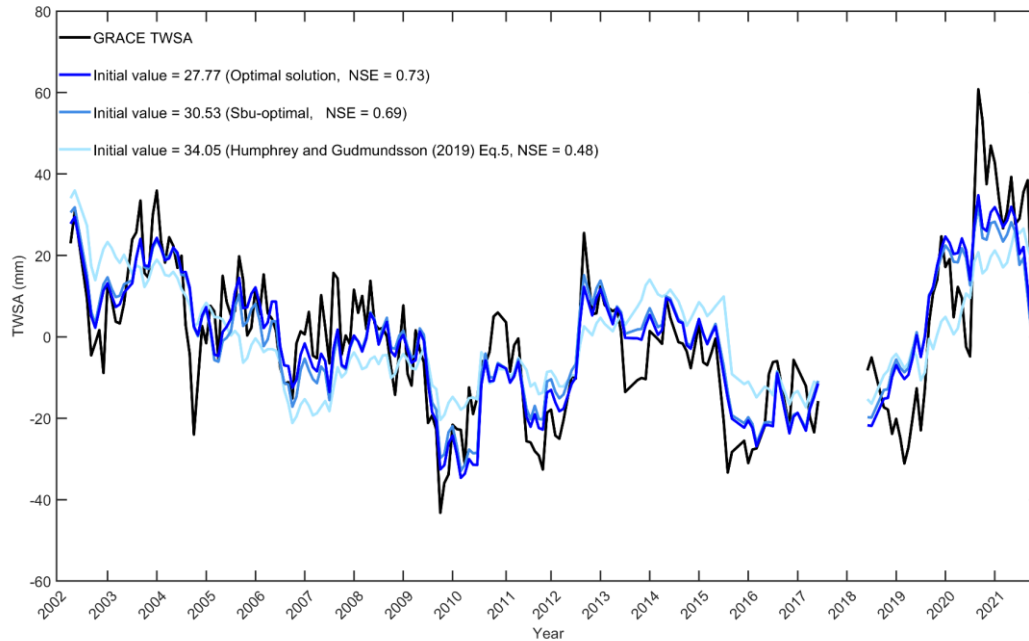
680

681

682 Figure 78: Spatial distribution of the difference in *NSE* between TWSA reconstructions forced by daily and
683 monthly meteorological data, with respect to GRACE JPLM from 2002 to 2021 (a). Time series of
684 GRACE/GRACE-FO TWSA and reconstructed TWSA (de-seasonalized and de-trended) using daily and monthly
685 meteorological data in the (b) Lena, (c) Yukon, (d) Yangtze, and (e) Amazon basins.

686 5.1.2 Sensitivity to Initial Conditions

687 This section investigates the influence of the initial terrestrial water storage, $TWS(0)$, on
688 reconstruction performance. Humphrey and Gudmundsson (2019) demonstrated through
689 experiments that if $TWS(0)$ is simply set to zero, the model requires a spin-up period before
690 reaching equilibrium. To avoid discarding multiple years of data, they derived an analytical
691 equilibrium value to serve as a uniform initialization for $TWS(0)$. However, when a basin is not in
692 climatic equilibrium, this equilibrium-based initialization can introduce systematic bias. Since the
693 model's memory decay coefficient ($c \cdot T_z + d$) is approximately equal to 1, such bias can persist
694 for several years in basins with long water residence times, making the initial condition a critical
695 factor influencing reconstruction accuracy in long-memory basins. To mitigate this bias, $TWS(0)$
696 in this study is jointly estimated along with the model parameters (a, b, c, d). Three initialization
697 strategies were compared (Fig. 89): (1) the optimal solution where $TWS(0)$ is treated as an
698 unknown and solved through least squares estimation; (2) a suboptimal solution, obtained by
699 increasing the optimal value by 10%; and (3) the equilibrium solution, derived from Eq. (5). Using
700 the Chad Basin as an example, the *NSE* of the equilibrium initialization was 0.48, which increased
701 to 0.57 under the suboptimal case and further improved to 0.73 under the globally optimal
702 initialization. Therefore, in this study, $TWS(0)$ is retrieved through parameter inversion for all
703 basins, substantially reducing systematic bias and enhancing reconstruction accuracy.



704

705 Figure 9: Time series of TWSA in the Chad Basin from GRACE observations and model reconstructions under
 706 three different initial condition strategies. GRACE data (black) are based on the JPLM; model reconstructions are
 707 obtained using (1) an optimized initialization (dark blue), (2) a sub-optimal initialization (medium blue), and (3)
 708 an equilibrium initialization following Eq. (5) of Humphrey and Gudmundsson (2019) (light blue).

709 5.2 Discussion of Parameter Sensitivity

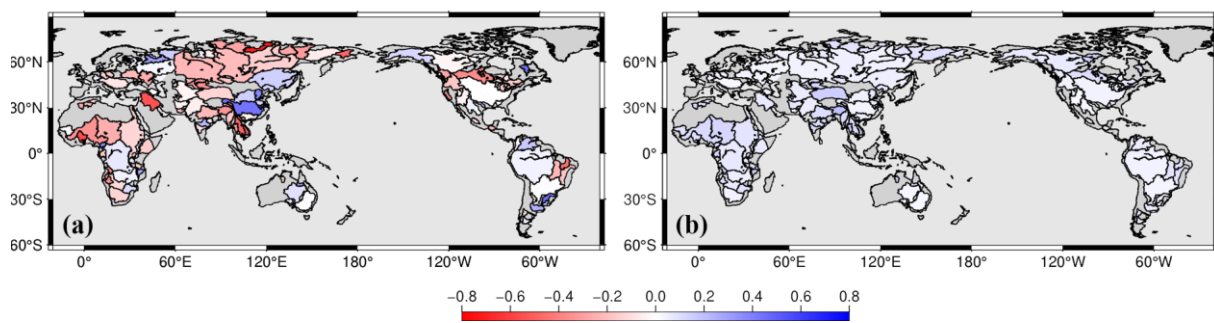
710 5.2.1 Parameter a

711 Figure 9–10 illustrates the global distribution of parameter a and its associated uncertainty.
 712 The spatial pattern of parameter a exhibits That parameter a arises from the first-order Taylor
 713 expansion of the temperature modulation term in the model formulation (Eq. 13). Therefore, it
 714 represents a mathematical sensitivity coefficient describing how temperature perturbs the
 715 relationship between precipitation input and TWS response. As shown in Fig. 10a, the sign of
 716 parameter a varies among basins, with positive values in some basins and negative values in others.
 717 In many high-latitude regions, the calibrated values tend to be negative, whereas some humid basins
 718 exhibit positive values. These spatial differences likely reflect variations in regional hydroclimatic
 719 conditions and the ways in which temperature influences hydrological processes such as snowmelt,
 720 evapotranspiration, and soil moisture dynamics. –pronounced contrasts across different climatic
 721 zones. In high-latitude cold regions, liquid runoff is nearly absent during winter, and when
 722 temperatures rise above 0 °C in summer, rapid snowmelt occurs. However, the presence of
 723 permafrost and surface ice layers greatly reduces infiltration capacity, causing meltwater to be
 724 discharged primarily as surface runoff rather than being retained in terrestrial water storage. As a

725 result, the inversion yields $a < 0$, indicating that warming diminishes the efficiency of precipitation
726 conversion into TWS.

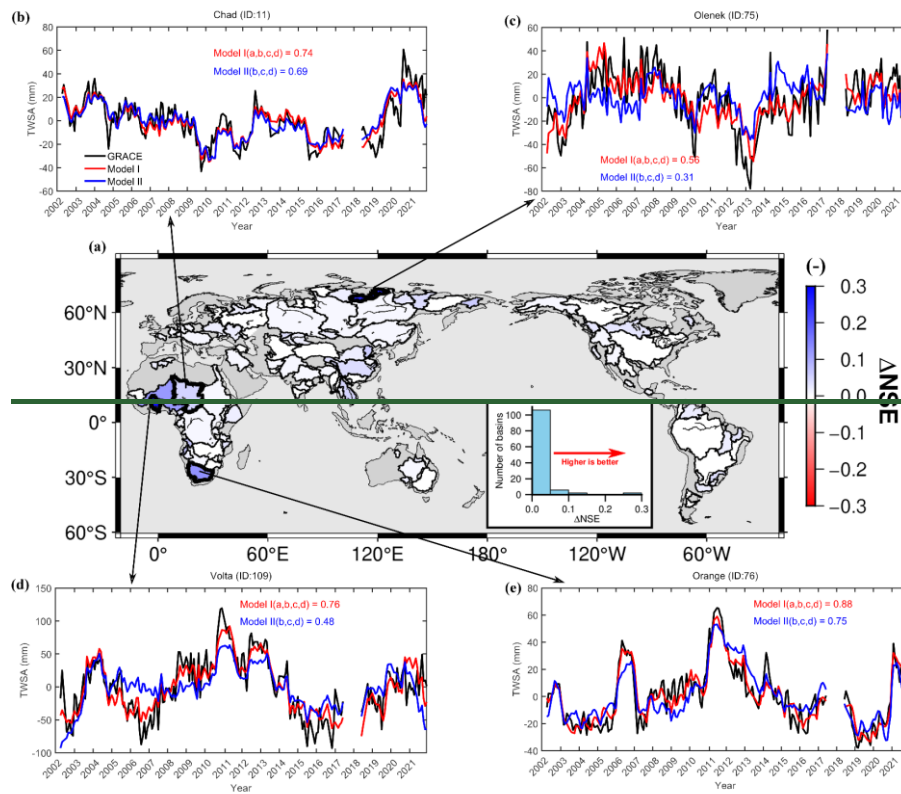
727 In low-latitude arid and semi-arid regions, the annual mean ET/P ratio is high (Fig. S5), and
728 evapotranspiration plays a dominant role in the water balance. As temperature increases, potential
729 evapotranspiration intensifies, leading to greater atmospheric loss of precipitation before infiltration,
730 which similarly results in $a < 0$. In contrast, the Yangtze River Basin exhibits a positive response
731 ($a > 0$), as warming coincides with the wet season and ET/P remains relatively low (Fig. S5). Under
732 these conditions, soil and vegetation can effectively retain and infiltrate rainfall, thereby enhancing
733 the conversion of precipitation into terrestrial water storage. Similarly, in the Yellow River Basin,
734 large-scale ecological restoration projects in recent years have substantially improved vegetation
735 cover, soil structure, and infiltration conditions, resulting in significant increases in both surface and
736 groundwater storage (Feng et al., 2025). Consequently, when temperatures rise and
737 evapotranspiration intensifies, the enhanced soil water retention and groundwater recharge are
738 sufficient to offset the additional evaporative losses. As a result, the model likewise yields a positive
739 response with $a > 0$.

740 Figure 10a-11a compares the full four-parameter model with a reduced three-parameter version
741 in which the temperature and precipitation coupling term (i.e., parameter a) is excluded. The global
742 distribution of ΔNSE indicates that, on average, the contribution of parameter a is limited.
743 However, under specific hydroclimatic conditions, incorporating parameter a can lead to
744 improvements in model performance with $\Delta NSE > 0.1$. Notable improvements are concentrated in
745 high-latitude snow-dominated basins, such as the Olenek River, and in certain arid regions with high
746 evapotranspiration, such as the Volta Basin. For the remaining 112 basins, ΔNSE values are below
747 0.1, suggesting no statistically significant difference. From a time series perspective, excluding
748 parameter a in the Volta Basin leads to an overestimation of summer peaks during 2005–2006 and
749 an underestimation during 2009–2012. In regions with high temperatures, removing parameter a
750 impairs the model's ability to capture interannual peak and trough variability.

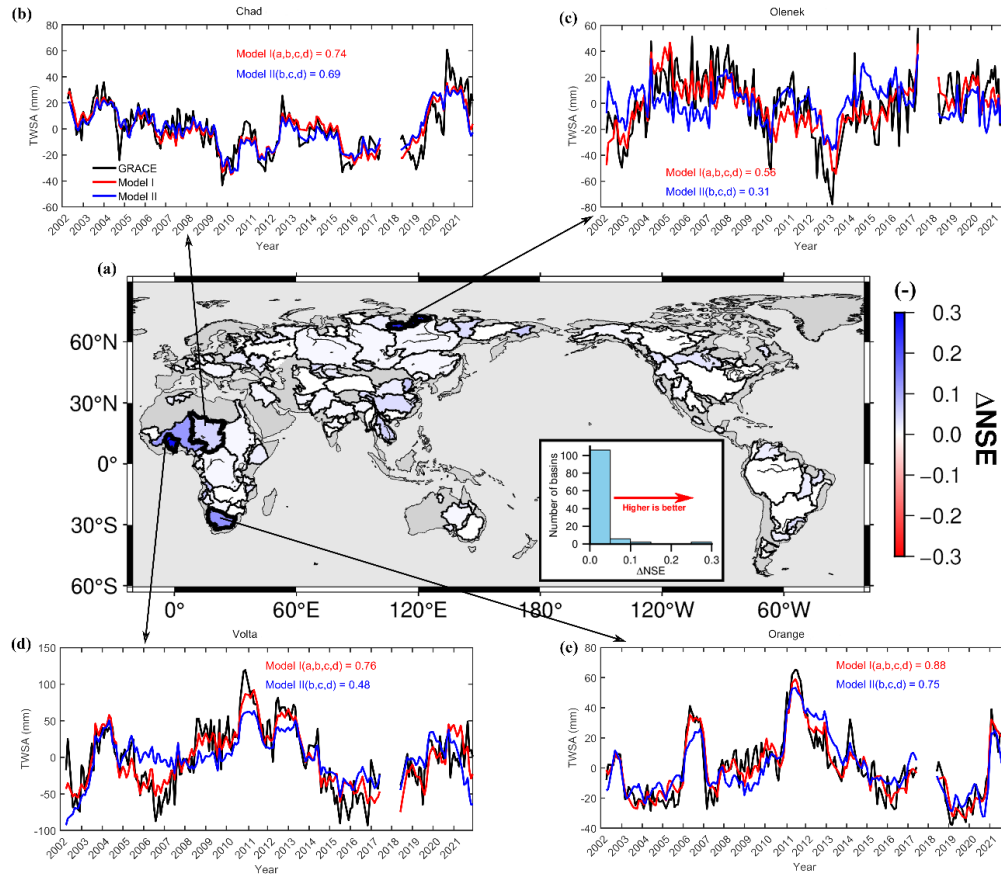


751

752 Figure 910: Spatial distribution of parameter a (a), and parameter a errors (b) across global 116 river basins.
 753 Parameters calibrated by monthly TWSA from JPLM based on ERA5-Land precipitation^P and temperature from
 754 2002 to 2021. Uncertainty estimation of parameters based on Monte Carlo simulations using precipitation and
 755 temperature errors across each basin. Precipitation errors were derived from the standard deviation between ERA5-
 756 Land and MSWEP datasets. Temperature errors were derived from the standard deviation between ERA5-Land
 757 and GLDAS-2.2 GLSM datasets.



758



759

760 Figure 11: Spatial distribution of the NSE difference between TWSA reconstructions from a four-parameter
 761 and a three-parameter (excluding parameter a) daily recursive model with respect to JPLM across 116 global
 762 river basins during 2002–2021 (a). Time series of GRACE/GRACE-FO TWSA and reconstructed TWSA (de-
 763 seasonalized and de-trended) in the (b) Chad, (c) Olenek, (d) Volta, and (e) Orange basins.

764

5.2.2 Parameter b

765

766

767

768

769

770

771

772

773

774

775

From Eq. (17) it follows that parameter b represents the fraction of precipitation that is ultimately converted into TWS: a larger b value indicates that a higher fraction of precipitation contributes to storage, whereas a smaller b suggests that a greater proportion of precipitation is dissipated through evapotranspiration or rapid runoff before becoming part of the basin water storage. In this sense, parameter b characterizes whether precipitation tends to be directly lost from the system or effectively retained as storage.

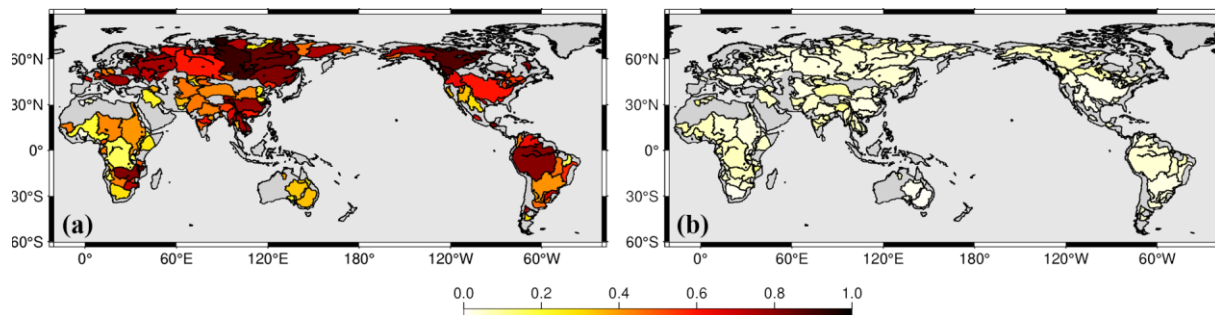
Figure 11–Figure 12 shows the global distribution of parameter b and its associated uncertainty. Overall, parameter b exhibits spatial heterogeneity across different regions. As shown in a Fig. 12, relatively low parameter b values are found in the Congo, Niger, and Orange River basins in Africa; the Lake Eyre and Murray basins in Australia; and the Rio Grande and Colorado basins in North America. These regions are characterized by relatively high long-term mean ET/P (Fig. S8); a large

776 fraction of precipitation is exhausted by evaporation and runoff before contributing to TWS , which
777 yields a low conversion efficiency. Consequently, the efficiency of precipitation-to-storage
778 conversion is low, resulting in smaller calibrated b values.

779 In contrast, higher b values are observed in high-latitude basins such as the Lena and Yenisey.
780 In these regions, winter precipitation is predominantly stored as snow or ice, delaying immediate
781 losses to the atmosphere or river discharge. During the snowmelt season, the accumulated solid
782 water is released and contributes to TWS . This storage–delay–release mechanism reduces the
783 fraction of direct precipitation loss and enhances the effective conversion of precipitation into TWS ,
784 thereby leading to higher b values.

785 To further substantiate this physical interpretation, we examined the statistical relationship
786 between parameter b and the multi-year mean loss ratio $(ET + R)/P$ at the basin scale (Fig. S9).
787 The results reveal a negative correlation between parameter b and $(ET + R)/P$. This statistical
788 relationship provides independent observational support for interpreting parameter b . Furthermore,
789 the global spatial pattern of b is consistent with the findings of (Zhong et al., 2025).

790 As illustrated, the spatial pattern of b is consistent with the findings of Zhong et al. (2025): high-
791 latitude regions, where winter snow accounts for a substantial portion of total precipitation, require
792 larger values of parameter b to compensate for the temporary storage effect of snow accumulation.
793 In arid and semi-arid basins across the mid- to low latitudes, ET/P ratios are generally high (Fig.
794 S5). As evapotranspiration dominates the depletion of shallow soil moisture, a substantial portion
795 of precipitation is lost to the atmosphere before it can infiltrate or recharge groundwater, resulting
796 in relatively low values of parameter b . In contrast, humid basins at similar latitudes exhibit lower
797 ET/P ratios, where only a small fraction of precipitation is consumed by evapotranspiration.
798 Consequently, a greater share of precipitation contributes to terrestrial water storage, leading to
799 higher b values.



801 Figure 12: Spatial distribution of parameter b (a), and parameter b errors (b) across global 116 river basins.
802 Parameters calibrated by monthly TWSA from JPLM based on ERA5-Land precipitation and temperature from
803 2002 to 2021. Uncertainty estimation of parameters based on Monte Carlo simulations using precipitation and
804 temperature errors across each basin. Precipitation errors were derived from the standard deviation between ERA5-
805 Land and MSWEP datasets. Temperature errors were derived from the standard deviation between ERA5-Land
806 and GLDAS-2.2 GLSM datasets.

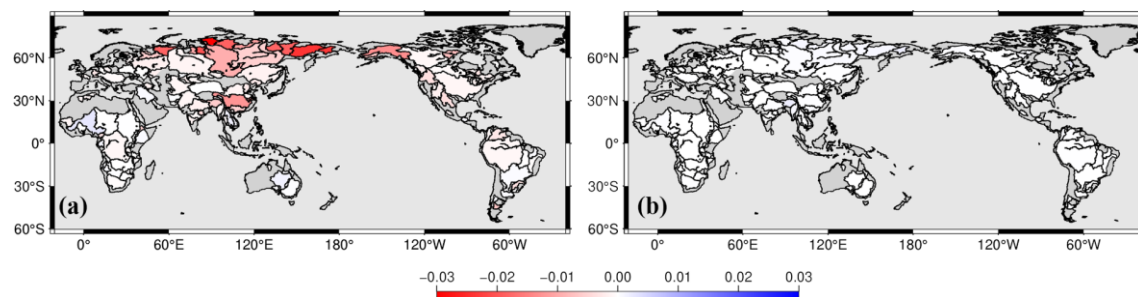
807 5.2.2.3 Parameter c

808 Figure 13 shows the global distribution of parameter c and its associated uncertainty.
809 The parameter c arises from the first-order Taylor expansion of the temperature modulation term
810 in the model formulation (Eq. 15). Therefore, it represents a mathematical sensitivity coefficient
811 describing how temperature perturbs the storage memory term. The parameter c exhibit clear
812 spatial variability. In many high-latitude basins, the magnitude of c is relatively larger (mostly
813 negative), whereas in most mid- and low-latitude basins the values are close to zero. This pattern
814 indicates that the influence of temperature on the model's water storage memory term is more
815 pronounced in colder regions, while in many other basins the recursive water storage component is
816 largely temperature-independent within our reconstruction model. In high-latitude basins,
817 parameter c is predominantly negative, indicating that rising temperatures substantially reduce the
818 contemporaneous water retention rate. This pattern aligns with typical high-latitude hydrological
819 processes: winter precipitation is stored in solid form and rapidly melts during spring warming,
820 resulting in surface runoff and a sharp decline in TWS. In contrast, low-latitude regions lack large-
821 scale snow accumulation and melt processes, resulting in weaker coupling between temperature and
822 the memory term. As a result, parameter c values in these regions are typically close to zero. The
823 spatial distribution of parameter uncertainty (Fig. 13b) further shows that estimation errors are
824 relatively small in most regions, suggesting that the adopted calibration approach is stable and robust
825 across the majority of basins.

826 Figure 14 compares the full four-parameter model with a reduced three-parameter
827 version excluding parameter c . Among the 116 basins analyzed, most exhibit limited sensitivity to
828 parameter c ; however, incorporating c still yields measurable performance improvements in some
829 cases, with 11 basins showing $\Delta NSE > 0.1$. Notable improvements are concentrated in high-
830 latitude cold regions around the Arctic (e.g., Yana, Yukon, and Lena), while limited improvements
831 are found in parts of North America (e.g., Columbia, Colorado, and Rio Grande) and in certain
832 Chinese basins (e.g., Yangtze and Yellow River).

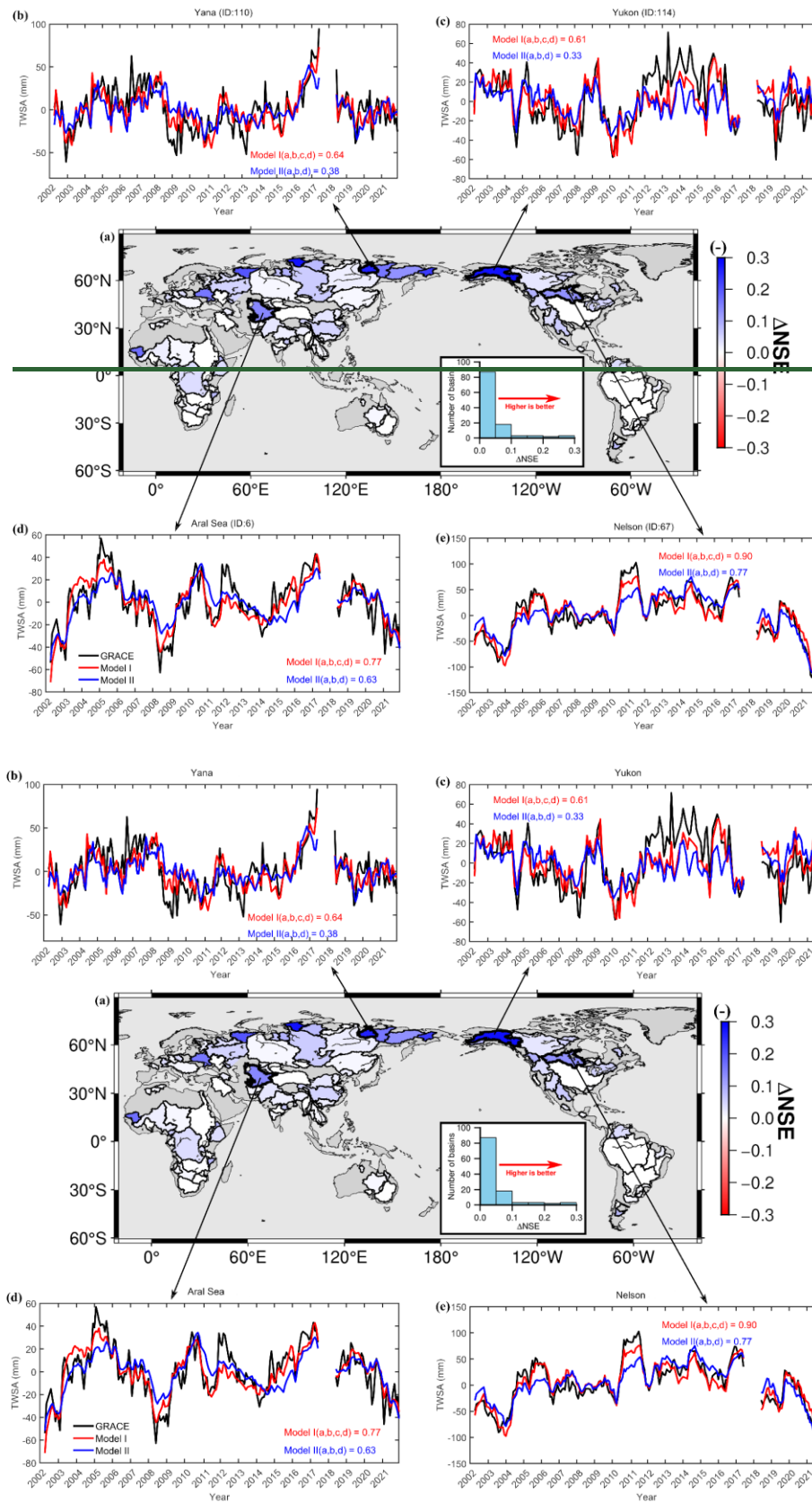
833 From a time series perspective, in the Yukon Basin, the average temperatures during the

834 snowmelt seasons of the period from 2006 to 2007 and in 2009 were markedly below normal (Fig.
835 [S103](#)). Under these conditions, the decay factor ($c \cdot T_z + d$) remained close to the baseline value
836 d , resulting in a slower dissipation rate. Meanwhile, SWE during these years was also below the
837 multi-year average, limiting the contribution from snowmelt. GRACE observations captured a slight
838 increase in TWS during spring, followed by a continuous decline. The four-parameter model
839 successfully reproduced this slow depletion process (Fig. [13e 14c](#)). In contrast, the three-parameter
840 model, due to the absence of a temperature modulation term, maintains a higher retention rate under
841 the same precipitation input and consequently produces an overall overestimation in the
842 reconstructed TWS curve. Conversely, 2019 was an exceptionally warm year, with precipitation
843 anomalies remaining positive from 2017 to 2021. Rising temperatures substantially reduce($c \cdot T_z +$
844 d), thereby accelerating the depletion of antecedent water storage. The abundant snowpack was
845 rapidly flushed during the melt season, resulting in a deeper TWS trough recorded by GRACE
846 compared to that of 2006 to 2007. The four-parameter model captured this deep trough due to the
847 dynamic weakening effect of the parameter c , whereas the three-parameter model produced a
848 shallower minimum. A similar pattern is observed in the Yana Basin: exceptionally high SWE in
849 2007 led to elevated TWS levels, while reduced snowmelt and elevated temperatures in the
850 following year (Fig. [S4S11](#)) triggered rapid snowmelt and a sharp decline in TWS during 2008. The
851 four-parameter model exhibits better agreement with GRACE observations, whereas the three-
852 parameter model shows excessive smoothing (Fig. [13b 14b](#)). These comparisons highlight the
853 critical role of the temperature modulation term c in accurately capturing TWS extremes during
854 warm years or periods of rapid snowmelt.



855

856 Figure 1213: Spatial distribution of parameter c (a), and parameter c uncertainties (b) across global 116 river
 857 basins.



858

859

860 Figure 14: Spatial distribution of the NSE difference between TWSA reconstructions from a four-parameter
861 and a three-parameter (excluding parameter c) daily recursive model with respect to JPLM across 116 global river
862 basins during 2002-2021 (a). Time series of GRACE/GRACE-FO TWSA and reconstructed TWSA (de-
863 seasonalized and de-trended) in the (b) Yana, (c) Yukon, (d) Aral Sea, and (e) Nelson basins.

864 5.2.3.4 Parameter d

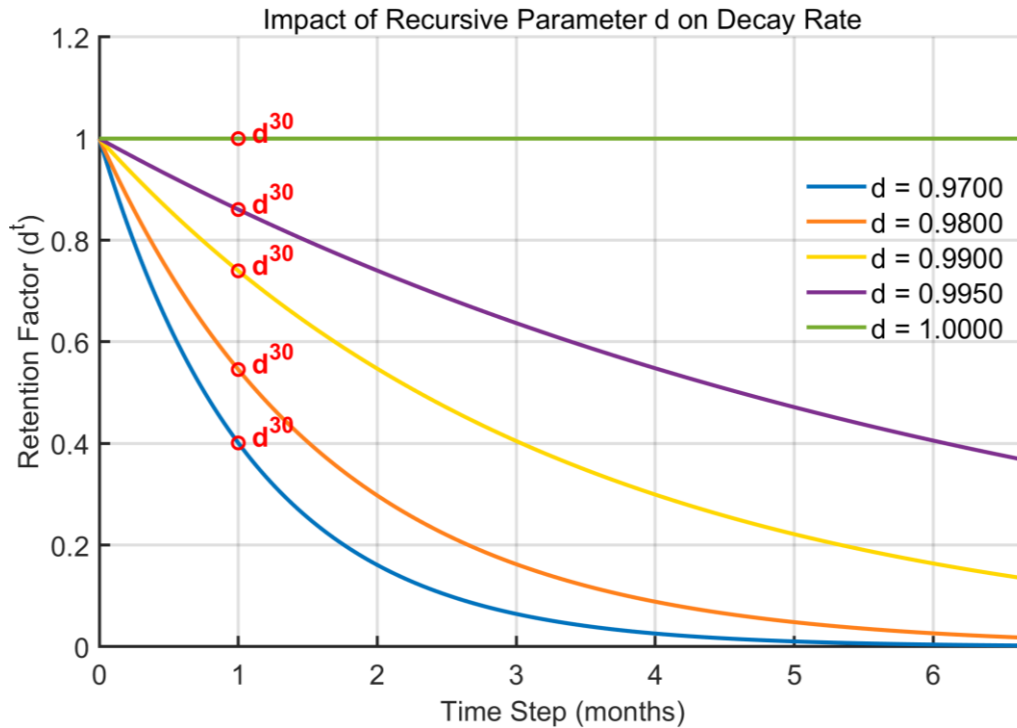
865 In the linear storage model, when no additional precipitation input is introduced, water
866 depletion follows an exponential decay process. As shown in Fig. 15, when ~~parameter~~ ~~the baseline~~
867 ~~memory coefficient~~ $d = 0.97$, and in the absence of both additional precipitation input and
868 temperature effects, only 40% of the stored water remains after one month. In contrast, when $d =$
869 0.99 , more than 70% of the stored water can still be retained after one month under the same
870 condition. This indicates that the interannual variability of TWS is highly sensitive to the value of
871 parameter d .

872 ~~To examine spatial variability, Fig. 16 presents~~ ~~Figure 15 presents~~ the global distribution of the
873 30-day retention factor (d^{30}) and its associated uncertainty (Fig. 16). ~~According to the model~~
874 ~~formulation, parameter d in Eq. (17) represents the fraction of antecedent storage that remains in~~
875 ~~the system after a period of decay. From Eq. (10) it follows that, when d approaches 1, the storage~~
876 ~~at the previous time step is almost entirely preserved, implying that the current total loss ($ET + R$)~~
877 ~~is primarily attributable to contemporaneous precipitation losses. Conversely, when d deviates~~
878 ~~from 1, current losses are also driven by the release of antecedent storage. This mechanism is~~
879 ~~consistent with the spatial pattern shown in Fig. 16a. In high-latitude regions of the Northern~~
880 ~~Hemisphere, the widespread presence of permafrost limits the infiltration of meltwater during the~~
881 ~~spring thaw, causing most of the water to be rapidly discharged as surface runoff. As a result, the~~
882 ~~calibrated parameter d baseline memory coefficient is relatively low, typically ranging from 0.98~~
883 ~~to 0.99. Although this value implies a faster daily decay rate, persistent snowfall during winter~~
884 ~~months largely compensates for water loss. When temperatures rise in spring, the negative value of~~
885 ~~parameter c quickly reduces the instantaneous retention rate, allowing the model to effectively~~
886 ~~capture the rapid recession of water storage observed by GRACE.~~

887 Notably, the Ob and Mackenzie River basins exhibit considerably higher water retention after
888 30 days of decay compared to other high-latitude basins (Fig. 16a). In the Ob basin,
889 approximately 15% of the upstream and midstream region between the Irtysh River and the upper
890 Ob is occupied by endorheic depressions, where inflow is retained and does not contribute to the
891 main channel (Yi et al., 2023). Additionally, springtime ice jams, channel backwater, and overbank
892 flooding further prolong the average residence time of water, resulting in a higher calibrated 30-day

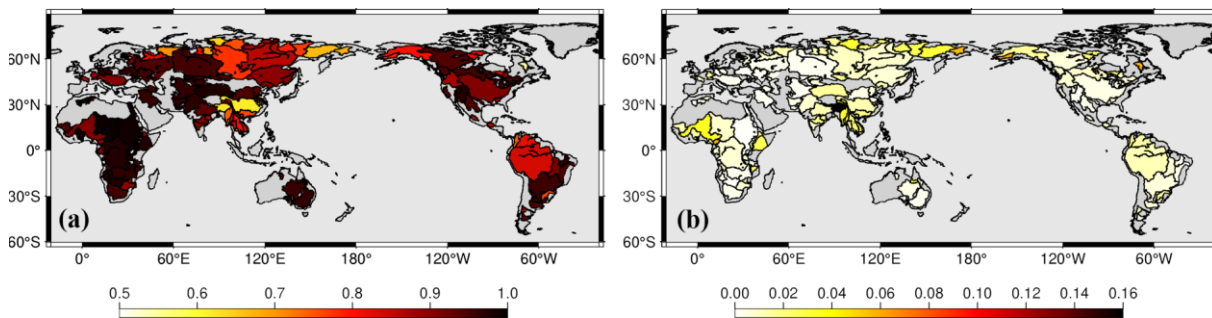
893 retention coefficient (d^{30}). In the Mackenzie basin, the presence of multiple large lakes leads to a
 894 highly fragmented river network (Yi et al., 2023), impeding the continuous drainage of liquid water
 895 and thereby extending the residence time of water within the basin.

896 ~~In contrast, tropical and subtropical basins are characterized by deep groundwater reservoirs~~
 897 ~~and long residence times, with no seasonal clearing effect from freeze and thaw processes. As a~~
 898 ~~result, the calibration favors higher values of parameter d (typically 0.995 to 0.998) to reproduce~~
 899 ~~the slow depletion of water storage over several months.~~



900

901 Figure 4415: Comparison of the temporal evolution of the decay factor under different values of parameter d (t
 902 in days).

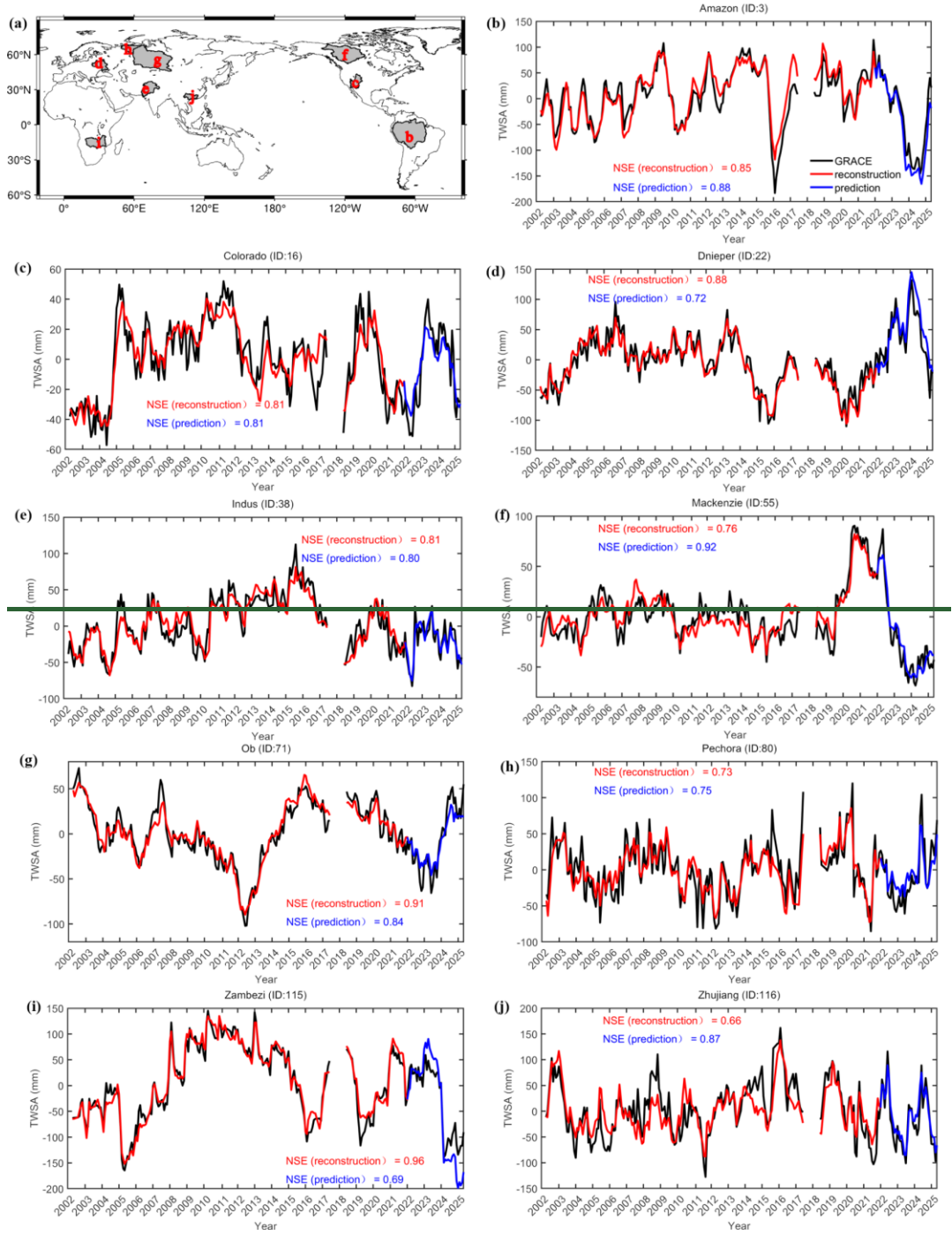


903

904 Figure 16: Spatial distribution of the 30-day retention factor d^{30} (a) and the uncertainty of parameter d^{30} (b)
905 across 116 global river basins.

906 **5.3 Model Extrapolation Evaluation**

907 In this study, model parameters were calibrated using GRACE data from 2002 to 2021 as the
908 training period. These parameters were then held constant to extrapolate TWSA for the period from
909 January 2022 to June 2025. To assess regional applicability, nine representative basins were selected
910 (Fig. 16), spanning high-latitude cold regions, tropical humid zones, and typical monsoon-affected
911 areas. For each basin, the predicted TWSA (blue line) was compared with the reconstructed values
912 during the training period (red line) and GRACE observations (black line). The results show that in
913 certain basins, such as the Amazon and Colorado, model performance during the extrapolation
914 period remained comparable to or even exceeded that during the training period. This indicates that
915 under these hydroclimatic conditions, the fixed-parameter model can reliably capture TWSA
916 variations driven by precipitation and temperature. For example, during the period from 2022 to
917 2024, the Amazon Basin experienced a severe extreme drought event (Fig. 16b). This event was
918 primarily driven by two factors: (1) a significant reduction in precipitation due to enhanced
919 atmospheric stability and suppressed convection; and (2) a persistent increase in atmospheric
920 evaporative demand under extreme high-temperature conditions (Fernández-Alvarez et al., 2025).
921 In some other basins, however, the predicted NSE dropped substantially. This decline may be
922 attributed to the limitations imposed by parameter nonstationarity and errors in the forcing data.
923 These results suggest that when only precipitation and temperature forecasts are available, the
924 proposed recursive model can be directly applied for estimating TWS changes during missing
925 periods or into the future. Nevertheless, its applicability varies with hydroclimatic conditions, and
926 for regions requiring high prediction accuracy, periodic parameter updates or the inclusion of
927 additional forcing information may still be necessary.



928

929 Figure 16: Time series of GRACE TWSA (black), reconstructed TWSA (red), and four-parameter climate-driven
 930 forecasts (blue) from January 2022 to May 2025 in nine basins (b-j). The global distribution of the nine selected
 931 river basins (a).

932 **5.4.3 Limitations of the study**

933 This approach relies on external precipitation and temperature forecasts for predicting future
 934 TWSA. In regions where precipitation and temperature forecasts are relatively accurate, the model
 935 is capable of producing reliable climate-driven TWSA predictions. Conversely, uncertainties in the

936 forcing data can significantly affect the reconstruction results. Therefore, both the applicability and
937 the upper limit of prediction accuracy are constrained by the quality of the forcing inputs. In addition,
938 the current model is designed to simulate deseasonalized and detrended TWSA only, and is not
939 capable of independently reproducing the full seasonal component or long-term trend.

940 In permafrost- and glacier-dominated basins, model performance is further limited. Taking the
941 Yukon Basin as an example (Fig. 6a), during the period from 2011 to 2014, the average temperatures
942 during the snowmelt seasons were significantly lower than normal for three consecutive years, while
943 annual precipitation slightly exceeded the long-term mean (Fig. [S3S10](#)). GRACE observations show
944 that TWSA remained at a consistently high level during this period, whereas our reconstruction
945 results are notably lower than those from GRACE. The primary source of error is likely associated
946 with the sub-daily freezing and thawing cycles within the snowpack, which is not explicitly
947 represented in the model. Meltwater generated during daytime warming is treated as immediate
948 runoff and removed from the system, while at night, when temperatures drop below 0 °C, a portion
949 of this water refreezes and is retained in the snowpack. Since the model does not incorporate this
950 refreezing into the subsequent day's initial storage, it systematically underestimates the net
951 accumulation within the snow layer. As a result, the peak in winter and spring is dampened, and the
952 overall reconstructed TWSA is biased low.

953

954 **6 Conclusions**

955 Building upon the classical linear water storage framework, this study introduces coupled
956 temperature and precipitation factors to develop a four-parameter daily recursive model for
957 reconstructing climate-driven TWSA at a $0.5^\circ \times 0.5^\circ$ spatial resolution over global land areas
958 (excluding Antarctica) for the period 2002–2021. The model is calibrated against the JPL RL06 and
959 GSFC RL06v2 mascon solutions, using hourly ERA5-Land precipitation and temperature data
960 aggregated to daily time steps as forcing inputs.

961 By treating $TWS(0)$ as an additional parameter to be estimated jointly with the other model
962 parameters, the influence of initial condition errors is substantially reduced, leading to improved
963 reconstruction accuracy. Independent calibrations conducted for 116 major river basins demonstrate
964 that the model parameters are more stable compared to existing approaches, while the reduced
965 number of calibration iterations significantly enhances computational efficiency. At the gridded
966 scale, the reconstruction closely aligns with GRACE/GRACE-FO mascon observations, with 62%
967 of grid cells achieving $NSE > 0.5$ for JPL-REC and 53% for GSFC-REC. A sensitivity analysis

968 further clarifies the physical interpretation of the four model parameters and their respective roles
969 in governing hydrological processes.

970 Comparison with existing statistical products demonstrates that the proposed model performs
971 well across multiple spatial scales. At the basin scale, reconstructed TWSA results were compared
972 with those from Zhong-REC. Among the 116 global river basins examined, 84 achieved a NSE
973 greater than 0.7 using the proposed model, whereas only 59 basins (51%) exceeded this threshold
974 with Zhong-REC. In most basins, the model yields improved performance, with the most substantial
975 gains observed in arid and semi-arid regions. At the gridded scale, the reconstructed results were
976 also compared with those from the Humphrey's model. After subtracting the Humphrey-JPL-REC
977 results from the JPL-REC reconstruction, 63% of the grid cells have ΔNSE values greater than
978 zero, indicating an overall improvement in model performance. The most pronounced improvements
979 are observed across the Arabian Peninsula and large parts of Africa.

980 At the daily scale, the reconstructed TWSA agrees well overall with the ITSG-Grace2018 daily
981 solution and GLDAS-2.2, indicating that the model can capture sub-monthly storage variability. The
982 reconstruction demonstrates comparable performance during independent training and validation
983 periods. The validation results show that about 60% of the basins retain NSE values greater than
984 0.5, and in representative basins such as the Amazon, Yangtze, Mississippi, and Murray, the
985 validation period reconstructions remain consistent with GRACE/GRACE-FO observations in both
986 amplitude and phase. These results indicate that the proposed framework does not exhibit overfitting
987 and has good temporal extrapolation capability.

988 In summary, this study develops a climate-driven model of global TWS variability at the
989 interannual scale, based on a simple four-parameter linear response framework that relies solely on
990 precipitation and temperature as inputs. This study introduces optimization strategies to improve
991 both computational efficiency and reconstruction accuracy. The method can be further extended to
992 incorporate additional factors such as wind speed, radiation, and topography, or to adopt nonlinear
993 relationships using machine learning approaches. However, the simplicity and high computational
994 efficiency demonstrated by the proposed framework greatly enhance its applicability and
995 interpretability. Future research will focus on simulating the seasonal and long-term trends of water
996 storage and ultimately aim to separate and quantify the relative impacts of climatic factors and
997 human activities on water resources across multiple temporal scales.

998

999 **Competing interests**

1000 The authors declare that they have no known competing financial interests or personal
1001 relationships that could have appeared to influence the work reported in this paper.
1002

1003 **Author contribution**

1004 P.X. conducted the data curation, formal analysis, and investigation; developed the model and
1005 software; and prepared the original manuscript draft. S.Y. conceptualized the study, acquired the
1006 funding, and supervised the research. Both authors contributed to the methodology and participated
1007 in the review and editing of the manuscript.

1008 **Acknowledgements**

1009 This research is funded by the National Natural Science Foundation of China (42374103,
1010 E214040201), the University of Chinese Academy of Sciences Research Start-up Grant
1011 (E3ER0402A2, 110400M003).
1012

1013 **Data availability**

1014 The authors are grateful to the NASA Goddard Space Flight Center
1015 (<https://earth.gsfc.nasa.gov/geo/data/grace-mascons>), ~~and the~~ Jet Propulsion Laboratory
1016 ([https://podaac.jpl.nasa.gov/dataset/TELLUS_GRAC-](https://podaac.jpl.nasa.gov/dataset/TELLUS_GRAC-GRFO_MASCON_CRI_GRID_RL06.1_V3)
1017 [GRFO_MASCON_CRI_GRID_RL06.1_V3](https://podaac.jpl.nasa.gov/dataset/TELLUS_GRAC-GRFO_MASCON_CRI_GRID_RL06.1_V3)), and the Center for Space Research, University of
1018 Texas at Austin (<http://www2.csr.utexas.edu/grace>) for providing the GRACE mascon solutions
1019 (last access: 31 July 2025). The authors thank Zhong et al. (2025) for providing publicly available
1020 datasets and source code that supported the reconstruction of terrestrial water storage anomalies,
1021 which are accessible from <https://doi.org/10.1038/s43247-024-01967-7>. The authors also are
1022 grateful for the water storage reconstruction dataset provided by Humphrey and Gudmundsson
1023 (2019) (<https://doi.org/10.6084/m9.figshare.7670849>). ERA5-Land precipitation, temperature and
1024 evapotranspiration datasets are provided by [https://doi.org/10.24381/cds.e2161bac](https://doi.org/10.24381/cds.e2161bac63)
1025 63(last access: 31 July 2025). MSWEP precipitation can be publicly obtained from [http://](http://www.gloh2o.org/mswep/65)
1026 www.gloh2o.org/mswep/65(last access: 31 July 2025). GLDAS-GLSM data can be publicly

1027 obtained from <https://disc.gsfc.nasa.gov/datasets> (last access: 31 July 2025). The boundary of global
1028 river basins is available at [https://www.bafg.de/SharedDocs/ExterneLinks/GRDC/mrb_shp_zip.
1029 html#62](https://www.bafg.de/SharedDocs/ExterneLinks/GRDC/mrb_shp_zip.html#62) (last access: 31 July 2025). Aridity index can be publicly obtained from
1030 <https://doi.org/10.6084/m9.figshare.7504448.v451> (last access: 31 July 2025).
1031

1032 **References**

- 1033 Abbott, B. W., Bishop, K., Zarnetske, J. P., Minaudo, C., Chapin, F. S., Krause, S., Hannah, D.
1034 M., Conner, L., Ellison, D., Godsey, S. E., Plont, S., Marçais, J., Kolbe, T., Huebner, A., Frei, R. J.,
1035 Hampton, T., Gu, S., Buhman, M., Sara Sayedi, S., Ursache, O., Chapin, M., Henderson, K. D., and
1036 Pinay, G.: Human domination of the global water cycle absent from depictions and perceptions, *Nat.*
1037 *Geosci.*, 12, 533-540, 10.1038/s41561-019-0374-y, 2019.
- 1038 An, L., Wang, J., Huang, J., Pokhrel, Y., Hugonnet, R., Wada, Y., Cáceres, D., Müller Schmied,
1039 H., Song, C., Berthier, E., Yu, H., and Zhang, G.: Divergent Causes of Terrestrial Water Storage
1040 Decline Between Drylands and Humid Regions Globally, *Geophys. Res. Lett.*, 48, e2021GL095035,
1041 <https://doi.org/10.1029/2021GL095035>, 2021.
- 1042 Baldocchi, D., Falge, E., Gu, L., Olson, R., Hollinger, D., Running, S., Anthoni, P., Bernhofer,
1043 C., Davis, K., and Evans, R.: FLUXNET: A new tool to study the temporal and spatial variability of
1044 ecosystem-scale carbon dioxide, water vapor, and energy flux densities, *Bull. Am. Meteorol. Soc.*,
1045 82, 2415-2434, 2001.
- 1046 Beck, H. E., van Dijk, A. I. J. M., Levizzani, V., Schellekens, J., Miralles, D. G., Martens, B.,
1047 and de Roo, A.: MSWEP: 3-hourly 0.25° global gridded precipitation (1979–2015) by merging
1048 gauge, satellite, and reanalysis data, *Hydrol. Earth Syst. Sci.*, 21, 589-615, 10.5194/hess-21-589-
1049 2017, 2017.
- 1050 Beck, H. E., Wood, E. F., Pan, M., Fisher, C. K., Miralles, D. G., van Dijk, A. I. J. M., McVicar,
1051 T. R., and Adler, R. F.: MSWEP V2 Global 3-Hourly 0.1° Precipitation: Methodology and
1052 Quantitative Assessment, *Bull. Am. Meteorol. Soc.*, 100, 473-500, [https://doi.org/10.1175/BAMS-
1053 D-17-0138.1](https://doi.org/10.1175/BAMS-D-17-0138.1), 2019.
- 1054 Burek, P. and Smilovic, M.: The use of GRDC gauging stations for calibrating large-scale
1055 hydrological models, *Earth Syst. Sci. Data*, 15, 5617-5629, 2023.
- 1056 Castle, S. L., Thomas, B. F., Reager, J. T., Rodell, M., Swenson, S. C., and Famiglietti, J. S.:
1057 Groundwater depletion during drought threatens future water security of the Colorado River Basin,
1058 *Geophys. Res. Lett.*, 41, 5904-5911, 2014.
- 1059 Chen, J., Cazenave, A., Dahle, C., Llovel, W., Panet, I., Pfeffer, J., and Moreira, L.:
1060 Applications and challenges of GRACE and GRACE follow-on satellite gravimetry, *Surv. Geophys.*,
1061 43, 305-345, 2022.
- 1062 Chen, J. L., Wilson, C. R., and Tapley, B. D.: The 2009 exceptional Amazon flood and
1063 interannual terrestrial water storage change observed by GRACE, *Water Resour. Res.*, 46, 2010.
- 1064 Chen, M., Shi, W., Xie, P., Silva, V. B., Kousky, V. E., Wayne Higgins, R., and Janowiak, J. E.:
1065 Assessing objective techniques for gauge - based analyses of global daily precipitation, *J. Geophys.*
1066 *Res.-Atmos.*, 113, 2008.
- 1067 Crochemore, L., Isberg, K., Pimentel, R., Pineda, L., Hasan, A., and Arheimer, B.: Lessons
1068 learnt from checking the quality of openly accessible river flow data worldwide, *Hydrol. Sci. J.*, 65,
1069 699-711, 2020.
- 1070 Duan, A., Zhong, Y., Xu, G., Yang, K., Tian, B., Wu, Y., Bai, H., and Hu, E.: Quantifying the

1071 2022 extreme drought in the Yangtze River Basin using GRACE-FO, *J. Hydrol.*, 630, 130680, 2024.
1072 Fan, C., Song, C., Liu, K., Ke, L., Xue, B., Chen, T., Fu, C., and Cheng, J.: Century - scale
1073 reconstruction of water storage changes of the largest lake in the inner Mongolia plateau using a
1074 machine learning approach, *Water Resour. Res.*, 57, e2020WR028831, 2021.
1075 Fekete, B. M., Looser, U., Pietroniro, A., and Robarts, R. D.: Rationale for monitoring
1076 discharge on the ground, *J. Hydrometeorol.*, 13, 1977-1986, 2012.
1077 Feng, J., Li, B., Song, J., Tang, B., Nyein, M. M., and Tani, B. P.: Spatiotemporal Variations of
1078 Terrestrial Water Storage and Driving Factors in the Water Towers of Northwest China Based on
1079 GRACE and Multi-Source Data Sets, *Water Resour. Res.*, 61, e2024WR039490,
1080 <https://doi.org/10.1029/2024WR039490>, 2025.
1081 Fernández-Alvarez, J. C., Nieto, R., Vicente-Serrano, S. M., Carvalho, D., and Gimeno, L.:
1082 Moisture and temperature sources were key drivers of the anomalies for the record-breaking of 2023
1083 Amazon drought, *Commun. Earth Environ.*, 6, 801, 10.1038/s43247-025-02771-7, 2025.
1084 Forootan, E., Khaki, M., Schumacher, M., Wulfmeyer, V., Mehrnegar, N., van Dijk, A. I.,
1085 Brocca, L., Farzaneh, S., Akinluyi, F., and Ramillien, G.: Understanding the global hydrological
1086 droughts of 2003–2016 and their relationships with teleconnections, *Sci. Total Environ.*, 650, 2587-
1087 2604, 2019.
1088 Gao, Y., Luo, Z., Liu, H., Wang, L., Chen, X., and Li, H.: Reconstruction of global long-term
1089 daily streamflow dataset using machine learning models for revealing streamflow changes, *Journal*
1090 *of Hydrology: Regional Studies*, 64, 103148, 2026.
1091 Humphrey, V. and Gudmundsson, L.: GRACE-REC: a reconstruction of climate-driven water
1092 storage changes over the last century, *Earth Syst. Sci. Data*, 11, 1153-1170, 10.5194/essd-11-1153-
1093 2019, 2019.
1094 Humphrey, V., Gudmundsson, L., and Seneviratne, S. I.: Assessing Global Water Storage
1095 Variability from GRACE: Trends, Seasonal Cycle, Subseasonal Anomalies and Extremes, *Surv.*
1096 *Geophys.*, 37, 357-395, 10.1007/s10712-016-9367-1, 2016.
1097 Humphrey, V., Rodell, M., and Eicker, A.: Using Satellite-Based Terrestrial Water Storage Data:
1098 A Review, *Surv. Geophys.*, 44, 1489-1517, 10.1007/s10712-022-09754-9, 2023.
1099 Laudon, H., Spence, C., Buttle, J., Carey, S. K., McDonnell, J. J., McNamara, J. P., Soulsby,
1100 C., and Tetzlaff, D.: Save northern high-latitude catchments, *Nat. Geosci.*, 10, 324-325, 2017.
1101 Li, B., Rodell, M., Kumar, S., Beaudoin, H. K., Getirana, A., Zaitchik, B. F., de Goncalves, L.
1102 G., Cossetin, C., Bhanja, S., Mukherjee, A., Tian, S., Tangdamrongsub, N., Long, D., Nanteza, J.,
1103 Lee, J., Policelli, F., Goni, I. B., Daira, D., Bila, M., de Lannoy, G., Mocko, D., Steele-Dunne, S. C.,
1104 Save, H., and Bettadpur, S.: Global GRACE Data Assimilation for Groundwater and Drought
1105 Monitoring: Advances and Challenges, *Water Resour. Res.*, 55, 7564-7586,
1106 <https://doi.org/10.1029/2018WR024618>, 2019.
1107 Li, F., Kusche, J., Chao, N., Wang, Z., and Löcher, A.: Long - term (1979 - present) total water
1108 storage anomalies over the global land derived by reconstructing GRACE data, *Geophys. Res. Lett.*,
1109 48, e2021GL093492, 2021.
1110 Li, F., Kusche, J., Rietbroek, R., Wang, Z., Forootan, E., Schulze, K., and Lück, C.: Comparison
1111 of data - driven techniques to reconstruct (1992 - 2002) and predict (2017 - 2018) GRACE - like
1112 gridded total water storage changes using climate inputs, *Water Resour. Res.*, 56, e2019WR026551,
1113 2020.
1114 Li, X., Jin, T., Liu, B., Chao, N., Li, F., and Cai, Z.: The Influence of ENSO on the Long -
1115 Term Water Storage Anomalies in the Middle - Lower Reaches of the Yangtze River Basin:
1116 Evaluation and Analysis, *Earth Space Sci.*, 10, e2023EA003007, 2023.
1117 Liu, B., Zou, X., Yi, S., Sneeuw, N., Cai, J., and Li, J.: Identifying and separating climate-and
1118 human-driven water storage anomalies using GRACE satellite data, *Remote Sens. Environ.*, 263,
1119 112559, 2021.

1120 Liu, B., Zou, X., Yi, S., Sneeuw, N., Li, J., and Cai, J.: Reconstructing GRACE-like time series
1121 of high mountain glacier mass anomalies, *Remote Sens. Environ.*, 280, 113177, 2022.

1122 Liu, X., Feng, X., Ciais, P., and Fu, B.: Widespread decline in terrestrial water storage and its
1123 link to teleconnections across Asia and eastern Europe, *Hydrol. Earth Syst. Sci.*, 24, 3663-3676,
1124 10.5194/hess-24-3663-2020, 2020.

1125 Long, D., Longuevergne, L., and Scanlon, B. R.: Global analysis of approaches for deriving
1126 total water storage changes from GRACE satellites, *Water Resour. Res.*, 51, 2574-2594, 2015.

1127 Long, D., Shen, Y., Sun, A., Hong, Y., Longuevergne, L., Yang, Y., Li, B., and Chen, L.:
1128 Drought and flood monitoring for a large karst plateau in Southwest China using extended GRACE
1129 data, *Remote Sens. Environ.*, 155, 145-160, 2014.

1130 Loomis, B., Luthcke, S., and Sabaka, T.: Regularization and error characterization of GRACE
1131 mascons, *Journal of geodesy*, 93, 1381-1398, 2019.

1132 Ma, N., Zhang, Y., and Szilagyi, J.: Water-balance-based evapotranspiration for 56 large river
1133 basins: A benchmarking dataset for global terrestrial evapotranspiration modeling, *J. Hydrol.*, 630,
1134 130607, 2024.

1135 Muñoz-Sabater, J.: ERA5-Land hourly data from 1981 to present, Copernicus climate change
1136 service (C3S) climate data store (CDS), 10, 2019.

1137 Muñoz-Sabater, J., Dutra, E., Agustí-Panareda, A., Albergel, C., Arduini, G., Balsamo, G.,
1138 Boussetta, S., Choulga, M., Harrigan, S., and Hersbach, H.: ERA5-Land: A state-of-the-art global
1139 reanalysis dataset for land applications, *Earth Syst. Sci. Data*, 13, 4349-4383, 2021.

1140 Ni, S., Chen, J., Wilson, C. R., Li, J., Hu, X., and Fu, R.: Global Terrestrial Water Storage
1141 Changes and Connections to ENSO Events, *Surv. Geophys.*, 39, 1-22, 10.1007/s10712-017-9421-7,
1142 2018.

1143 Palazzoli, I., Ceola, S., and Gentile, P.: GRACE: reconstructing terrestrial water storage
1144 anomalies with recurrent neural networks, *Sci. Data*, 12, 146, 2025.

1145 Pastorello, G., Trotta, C., Canfora, E., Chu, H., Christianson, D., Cheah, Y.-W., Poindexter, C.,
1146 Chen, J., Elbashandy, A., and Humphrey, M.: The FLUXNET2015 dataset and the ONEFlux
1147 processing pipeline for eddy covariance data, *Sci. Data*, 7, 225, 2020.

1148 Riegger, J. and Tourian, M. J.: Characterization of runoff - storage relationships by satellite
1149 gravimetry and remote sensing, *Water Resour. Res.*, 50, 3444-3466, 2014.

1150 Rodell, M., Velicogna, I., and Famiglietti, J. S.: Satellite-based estimates of groundwater
1151 depletion in India, *Nature*, 460, 999-1002, 2009.

1152 Rodell, M., Famiglietti, J. S., Wiese, D. N., Reager, J., Beaudoin, H. K., Landerer, F. W., and
1153 Lo, M.-H.: Emerging trends in global freshwater availability, *Nature*, 557, 651-659, 2018.

1154 Save, H., Bettadpur, S., and Tapley, B. D.: High - resolution CSR GRACE RL05 mascons,
1155 *Journal of Geophysical Research: Solid Earth*, 121, 7547-7569, 2016.

1156 Sun, A. Y., Scanlon, B. R., Save, H., and Rateb, A.: Reconstruction of GRACE total water
1157 storage through automated machine learning, *Water Resour. Res.*, 57, e2020WR028666, 2021.

1158 Sun, Z., Long, D., Yang, W., Li, X., and Pan, Y.: Reconstruction of GRACE data on changes in
1159 total water storage over the global land surface and 60 basins, *Water Resour. Res.*, 56,
1160 e2019WR026250, 2020.

1161 Tapley, B. D., Watkins, M. M., Flechtner, F., Reigber, C., Bettadpur, S., Rodell, M., Sasgen, I.,
1162 Famiglietti, J. S., Landerer, F. W., and Chambers, D. P.: Contributions of GRACE to understanding
1163 climate change, *Nature climate change*, 9, 358-369, 2019.

1164 Tian, K., Wang, Z., Li, F., Gao, Y., Xiao, Y., and Liu, C.: Drought Events over the Amazon
1165 River Basin (1993–2019) as Detected by the Climate-Driven Total Water Storage Change, *Remote
1166 Sens.*, 13, 1124, 2021.

1167 Trabucco, A. and Zomer, R. J.: Global Aridity Index and Potential Evapotranspiration (ET0)
1168 Climate Database v3, International Center for Tropical Agriculture (CIAT) and World Agroforestry

1169 Centre (ICRAF) [dataset], 10.6084/m9.figshare.7504448.v3, 2019.

1170 Voss, K. A., Famiglietti, J. S., Lo, M., De Linage, C., Rodell, M., and Swenson, S. C.:
1171 Groundwater depletion in the Middle East from GRACE with implications for transboundary water
1172 management in the Tigris - Euphrates - Western Iran region, *Water Resour. Res.*, 49, 904-914, 2013.

1173 Wiese, D., Yuan, D., Boening, C., Landerer, F. W., and Watkins, M.: JPL GRACE and GRACE-
1174 FO Mascon Ocean, Ice, and Hydrology Equivalent Water Height Coastal Resolution Improvement
1175 (CRI) Filtered Release 06 Version 02, DAAC: Pasadena, CA, USA, 2019.

1176 Xiao, C., Zhong, Y., Wu, Y., Zhang, Z., Bai, H., and Li, Z.: Flood Evolution in the Past 60 Years
1177 Revealed by Reconstructed Daily Terrestrial Water Storage Anomalies in China, *Water Resour. Res.*,
1178 61, e2024WR038712, <https://doi.org/10.1029/2024WR038712>, 2025.

1179 Xu, L., Chen, N., Moradkhani, H., Zhang, X., and Hu, C.: Improving global monthly and daily
1180 precipitation estimation by fusing gauge observations, remote sensing, and reanalysis data sets,
1181 *Water Resour. Res.*, 56, e2019WR026444, 2020.

1182 Yi, S., Saemian, P., Sneeuw, N., and Tourian, M. J.: Estimating runoff from pan-Arctic drainage
1183 basins for 2002–2019 using an improved runoff-storage relationship, *Remote Sens. Environ.*, 298,
1184 113816, 2023.

1185 Yi, S., Sun, W., Feng, W., and Chen, J.: Anthropogenic and climate-driven water depletion in
1186 Asia, *Geophys. Res. Lett.*, 43, 9061-9069, <https://doi.org/10.1002/2016GL069985>, 2016.

1187 Yin, J., Slater, L. J., Khouakhi, A., Yu, L., Liu, P., Li, F., Pokhrel, Y., and Gentine, P.: GTWS-
1188 MLrec: global terrestrial water storage reconstruction by machine learning from 1940 to present,
1189 *Earth Syst. Sci. Data*, 15, 5597-5615, 2023.

1190 Zhang, D., Zhang, Q., Werner, A. D., and Liu, X.: GRACE-based hydrological drought
1191 evaluation of the Yangtze River Basin, China, *J. Hydrometeorol.*, 17, 811-828, 2016.

1192 Zhang, J., Liesch, T., and Goldscheider, N.: Impacts of climate change and human activities on
1193 global groundwater storage from 2003 to 2022, *J. Hydrol.*, 664, 134298,
1194 <https://doi.org/10.1016/j.jhydrol.2025.134298>, 2025.

1195 Zhang, L. and Sun, W.: Progress and prospect of GRACE Mascon product and its application,
1196 *Reviews of Geophysics and Planetary Physics*, 53, 35-52, 2022.

1197 Zhang, Z., Chao, B., Chen, J., and Wilson, C.: Terrestrial water storage anomalies of Yangtze
1198 River Basin droughts observed by GRACE and connections with ENSO, *Glob. Planet. Change*, 126,
1199 35-45, 2015.

1200 Zheng, S., Zhang, Z., Yan, H., Zhao, Y., and Li, Z.: Characterizing drought events occurred in
1201 the Yangtze River Basin from 1979 to 2017 by reconstructing water storage anomalies based on
1202 GRACE and meteorological data, *Sci. Total Environ.*, 868, 161755,
1203 <https://doi.org/10.1016/j.scitotenv.2023.161755>, 2023.

1204 Zhong, Y., Feng, W., Humphrey, V., and Zhong, M.: Human-Induced and Climate-Driven
1205 Contributions to Water Storage Variations in the Haihe River Basin, China, *Remote Sens.*, 11, 3050,
1206 2019.

1207 Zhong, Y., Tian, B., Kim, H., Yuan, X., Liu, X., Zhu, E., Wu, Y., Wang, L., and Wang, L.: Over
1208 60% precipitation transformed into terrestrial water storage in global river basins from 2002 to 2021,
1209 *Commun. Earth Environ.*, 6, 53, 2025.

1210 Zomer, R. J., Xu, J., and Trabucco, A.: Version 3 of the Global Aridity Index and Potential
1211 Evapotranspiration Database, *Sci. Data*, 9, 409, 10.1038/s41597-022-01493-1, 2022.

1212